Dynamical aspects of photoionization from the $1s^2 2snp\,{}^1P_1^o$ levels belonging to the C III ion near the first ionization threshold

Cristian Iorga *

National Institute for Laser, Plasma, and Radiation Physics, Atomistilor 409, P.O. Box MG-36, Magurele-Ilfov 077125, Romania and University of Bucharest, Faculty of Physics, Atomiştilor 405, CP-MG 11, Măgurele-Bucharest 077125, Romania

(Received 16 November 2022; revised 25 January 2023; accepted 2 March 2023; published 21 March 2023)

This paper presents time-dependent Dirac calculations for femtosecond laser-driven single-photon ionization of $1s^2 2snp\,{}^1P_1^o$ states belonging to the C III ion, with $n \leqslant 5$, near the first ionization threshold. Increasing the field intensity broadens the photoelectron spectral distribution, pushing the lower energetic tail into the forbidden region below threshold. The energy domain cutoff condition leads to the formation of nonlocal temporal terms in the evolution of atomic states. These terms effectively give rise to discrete-continuum Rabi oscillations consisting in cycles of pulsed photoionization and stimulated radiative recombination processes, suppressing the electron yield and modulating the spectral distribution into multipeak structures. Field intensity scaling with photoelectron energy restricts these oscillations to near-threshold photoionization. These effects become relevant as state-of-the-art lasers provide shorter pulses designed to monitor electron dynamics at their natural timescales in various chemical reactions or physical processes.

DOI: 10.1103/PhysRevA.107.033115

I. INTRODUCTION

Photoionization of few-electron ions is an important test case for probing nonlinear phenomena [1,2], investigating many-body [3] and correlation [4,5] effects in atomic physics. Rohringer and Santra [6,7] showed that by resonantly tuning the laser field frequency to the $1s$-$3p$ transition in atomic neon, a strong-field-induced resonant Auger process occurs and leads to various asymmetries in the emitted electron spectra. Demekhin and Cederbaum studied the interference between direct and resonant photoionization processes [8] and further explored the dynamics between closely lying resonances interacting through continuum channels [9] by employing the local approximation [10,11]. These approaches provide semiclassical descriptions of field-induced dynamics for resonant Auger and photoionization processes; however, adaptation to different atomic systems is not trivial.

Dias *et al.* [4] showed that the independent-particle model is no longer valid in the case of photoionization at high energies from nl subshells with $l > 0$ belonging to atomic neon due to coupling with ns-type channels. This was further confirmed for photoionization from different subshells in atomic krypton [12] and xenon [13]. Furthermore, spin polarization of energetic photoelectrons was shown to be significantly more sensitive to the interchannel coupling compared to the photoionization cross section [14]. The difference between dynamic polarization of bound and continuum electronic states governs the dynamic interference in photon-atom interactions as demonstrated by Baghery *et al.* [15]. Photoionization dynamics of atomic orbitals outside the K shell is significantly affected by correlation effects associated with new open channels irrespective of photon energy.

Alternatively, at low photon energies, barely able to single-photon ionize above the threshold, there are several major issues that need to be addressed. First, the continuum wave functions vary rapidly with photoelectron energy, giving rise to further difficulties in decoupling the time evolution of discrete from continuum states in the photoionization dynamics. This behavior is imprinted on the one- and two-body radial integrals, e.g., on the electric dipole and Coulomb matrix elements, respectively. Schippers *et al.* [16] showed how a small deviation of 100 meV in the resonance position near the threshold leads to a value 2.7 times higher for the dielectronic recombination rate coefficients of Be-like Mg IX for a temperature range corresponding to the maximum abundance of this ion in photoionized gas. A similar finding was observed in the Xe-like W^{20+} ion [17] near the first ionization threshold where the dielectronic recombination rate coefficient used for modeling magnetized plasmas had been overestimated by a factor 4 [18]. Fortunately, this energy dependence of bound-free interaction terms becomes smoother at higher electron energies [19,20].

Second, a lower photoelectron energy corresponds to a higher timescale, which may become comparable to the duration of modern-day tabletop lasers leading to nonlinear effects. Such effects occur in attosecond laser streaking where the photoelectron emission is time delayed [21,22] and the corresponding spectra present complex interference patterns [23].

Finally, low-energy or thermal electrons have a higher chance of being subjected to the laser-field-induced radiative recombination [24–26], the inverse process of pulsed photoionization. The former occurs when open channels can resonantly couple to a bound state in the presence of an external laser field. Field stimulation leads to enhancement of up to three orders of magnitude compared to the spontaneous radiative recombination rate in the case of H^+ and He^+ ions

*iorga.cristian@inflpr.ro

[27]. However, the gain factor for this process scales with laser frequency as ν^{-3}, indicating that this type of recombination process is indeed more probable for low-energy electrons.

Mannervik *et al.* [28] accurately measured the strong autoionizing $1s^2 2p4l\ ^{1,3}L$ states belonging to C^{2+} by performing a dielectronic recombination experiment at the CRYRING ion storage facility [29]. The results are consistent with the configuration-interaction (CI) many-body perturbation theory (MBPT) approach of Derevianko *et al.* [30]. These quasibound states are situated in the 0–0.6 eV range above the first ionization threshold $1s^2 2s\ ^2S^e_{1/2}$ and have been intensively studied in the literature [31–40]. They may form resonances in the cross sections corresponding to photoionization of the C^{2+} ion [41–46], electronic impact excitation [47,48], and recombination [49–53] of C^{3+}. Other works performed unified treatments of previously mentioned atomic processes [54,55] containing said resonances. The $1s^2 2p4p\ ^1S^e_0$ quasibound state gives rise to a strong resonance in the photoionization of $1s^2 2s2p\ ^1P^o_1$ [45] and its position relative to threshold (485 meV) is comparable to its decay width (221 meV) [28], making it ideal for exploring threshold effects. The $1s^2 2snp\ ^1P^o_1$ levels are of considerable interest in atomic physics and experimentally accessible by pumping the ground state of C III with XUV radiation [56].

The C^{2+} ion is a suitable test candidate for investigating threshold effects on the pulsed laser-driven single-photon ionization of $1s^2 2snp\ ^1P^o_1$ due to its limited number of autoionizing states situated just above the first threshold with their relative positions being comparable to their corresponding decay widths. This work is structured as follows. The following section describes the theoretical approach starting with the atomic model for the C^{2+} ion by employing the Dirac-Fock-Slater model-potential method and then provides the evolution of expansion coefficients by solving the time-dependent Dirac equation. Section III contains structure results such as energy levels and bound-bound, bound-(quasi)bound, bound-free, and (quasi)bound-free electric dipole matrix elements together with autoionization amplitudes and rates. Section IV provides the time-dependent calculations of field-induced dynamics in the photoionization of $1s^2 2snp\ ^1P^o_1$ levels belonging to the C^{2+} ion. Section V gives the concluding remarks of this work.

II. THEORETICAL APPROACH

In the electric dipole approximation, photoionization from $1s^2 2snp\ ^1P^o_1$ levels only populates open channels of total angular momentum $J = 0, 1, 2$ and even parity. Since single-photon ionization is assumed to occur below the second ionization threshold, the only possible final states are formed by coupling the Li-like $1s^2 2s\ ^2S^e_{1/2}$ target state to a free electron respecting angular momentum addition rules and parity conservation.

The photoionization process in this work comprises a direct and a two-step resonant pathway as shown in the scheme

$$1s^2 2snp\left(^1P^o_1\right) + h\nu \rightarrow [1s^2 2s(^2S^e_{1/2}) + \epsilon s, d]\left(^{1,3}L^e_J\right) \searrow 1s^2 2p4l\left(^{1,3}L^e_J\right) \nearrow, \quad (1)$$

TABLE I. Partial symmetries and resonance contributions in the photoionization of $1s^2 2snp(^1P^o_1)$ states, with $2 \leqslant n \leqslant 5$.

Partial symmetries	Intermediate states	*LSJ* notation	Final states
$J^\pi = 0^e$	$(2p_{3/2}4p_{3/2})^e_0$	$2p4p\ ^1S^e_0$	$(2s_{1/2}\epsilon s_{1/2})^e_0$
$J^\pi = 1^e$	$(2p_{3/2}4f_{5/2})^e_1$	$2p4f\ ^3D^e_1$	$(2s_{1/2}\epsilon s_{1/2})^e_1$
			$(2s_{1/2}\epsilon d_{3/2})^e_1$
$J^\pi = 2^e$	$(2p_{1/2}4f_{5/2})^e_2$	$2p4f\ ^3F^e_2$	$(2s_{1/2}\epsilon d_{3/2})^e_2$
	$(2p_{3/2}4f_{5/2})^e_2$	$2p4f\ ^3D^e_2$	$(2s_{1/2}\epsilon d_{5/2})^e_2$
	$(2p_{3/2}4f_{7/2})^e_2$	$2p4f\ ^1D^e_2$	

where the *LSJ* notation is used. The resonant pathway consists of photoexcitation via an external laser field of state $1s^2 2snp\ ^1P^o_1$ to a quasibound level $1s^2 2p4l\ ^{1,3}L^e_J$, which autoionizes to open channels of symmetries similar to those of the intermediate level. This scheme contains a handful of such autoionizing states with symmetries $J^\pi = 0^e, 1^e, 2^e$ situated between the first and second ionization thresholds [28,30] as shown in Table I.

According to Mannervik *et al.* [28], these particular quasibound states are situated at less than 0.5 eV relative to the first threshold. The binding energy (994.465 eV) and ionization potential (47.887 78 eV) for C III, as provided by NIST [57], help estimate the energies of $1s^2 2p4l$ autoionizing states around the -946.1 eV value. The first-order relativistic correction to single-particle orbital energy is proportional to $\alpha^2 Z^2 \approx 0.05\%$ in the case of the C III ion, where $\alpha \approx 1/137.036$ is the fine-structure constant and $Z \approx 3$ is the effective nuclear screened charge experienced by one electron. A gross estimation of the relativistic contribution to the $1s^2 2p4l$ states amounts to 0.5 eV. Since the energy of quasibound states relative to the threshold is less than 0.5 eV, relativistic corrections are more than capable of interchanging high-lying bound levels with discrete autoionizing states. Hence, relativistic effects play a fundamental role when calculating resonance structures near ionization thresholds, even in the case of light elements such as carbon.

The relativistic effects can be accounted for by using a Breit-Pauli Hamiltonian in intermediate coupling or by solving the Dirac equation in jj coupling. In the present work, the discrete bound and autoionization states are described within the Dirac-Fock-Slater model potential and the continuum orbitals are computed by employing the distorted-wave approximation. Resonances are treated perturbatively in the scattering process. Atomic units are used unless stated otherwise.

A. Atomic model

The atomic configuration state functions (CSFs) have been determined using the Dirac-Fock-Slater model-potential approach implemented in flexible atomic code (FAC) [58]. Bound-free processes comprising resonance structures have been previously treated [59,60] within this approach. The stationary Dirac Hamiltonian for the Be-like C^{2+} atomic system is given by

$$H_0 = \sum_{i=1}^{4} \left(c\vec{\alpha}_i \cdot \vec{p}_i + \beta_i mc^2 - \frac{Z}{r_i} \right) + \sum_{i<j} \frac{1}{r_{ij}}. \quad (2)$$

In the absence of a mutual electronic interaction, the single-particle wave function is a quadrivector of type

$$\phi_{n,\kappa,m}(r,\theta,\varphi) = \frac{1}{r}\begin{pmatrix} \mathcal{P}_{n,\kappa}(r)\chi_{\kappa,m}(\theta,\varphi) \\ i\mathcal{Q}_{n,\kappa}(r)\chi_{-\kappa,m}(\theta,\varphi)\end{pmatrix}, \tag{3}$$

where $\kappa = (l-j)(2j+1)$ is the relativistic angular quantum number. The spin-angular functions $\chi_{\kappa,m}$ are given by

$$\chi_{\kappa,m}(\theta,\varphi) = \sum_{m_s=-1/2}^{1/2} \mathcal{C}^{\,l\ \ 1/2\ j}_{m-m_s\ m_s\ m}\, Y_l^{m-m_s}(\theta,\varphi)\xi_{m_s}, \tag{4}$$

where $\mathcal{C}^{\,l\ \ 1/2\ j}_{m-m_s\ m_s\ m}$ is the Clebsch-Gordan coefficient, $Y_l^{m-m_s}(\theta,\varphi)$ is the spherical harmonic, and ξ_{m_s} are the up and down spinors.

The CSFs denoted by $\Phi(\mu J\pi)$ are formed as antisymmetric products of single-particle orbitals. Flexible atomic code performs the Dirac-Fock-Slater iteration on a fictitious mean configuration determining the average potential and single-particle orbitals, which are then used to compute the energies E_μ^{av} of each and every CSFs. The mean configuration is obtained by distributing the active electron within the states of interest; hence some orbitals may contain fractional occupational numbers. A configuration interaction is implemented by diagonalizing the Hamiltonian matrix constructed within configuration space. The latter step provides mixing coefficients and new energy levels accounting for correlation effects. By suppressing the magnetic numbers, the final wave functions are given as superpositions of CSFs with the same $J\pi$ symmetry,

$$\Psi(\nu J\pi) = \sum_{\mu=1}^{N_c} b_{\nu\mu}\Phi(\mu J\pi), \quad 1 \leqslant \mu,\nu \leqslant N_c, \tag{5}$$

where $b_{\nu\mu}$ are mixing coefficients and N_C is the total number of CSFs with $J\pi$ symmetry. Flexible atomic code applies a procedure to mitigate the errors in energy caused by using a single potential optimized to a (mean) configuration. Prior to diagonalization, the central potential is optimized for each individual CSF and used to determine its energy E_μ^O. The difference $\Delta E_\mu = E_\mu^O - E_\mu^{av}$ is applied to the final diagonalized energies $E_\mu^d + \Delta E_\mu$.

In order to treat the ionization processes one needs to form open channels by coupling Li-like target states $|f^+ m_f\rangle$ to single-particle free-electron orbitals $|\epsilon\kappa m_e\rangle$. The latter are obtained by solving the Dirac equation using the average potential calculated based on the mean configuration. The coupled states are then given by

$$|f^+,\epsilon\kappa;JM\pi\rangle = \sum_{m_f m_e} \mathcal{C}^{\,j_f\ \ j_e\ \ J}_{m_f\ m_e\ M}|f^+ m_f\rangle \otimes |\epsilon\kappa m_e\rangle. \tag{6}$$

Radial orbitals corresponding to continuum electrons given by FAC are further divided by $\sqrt{\pi}$ in order to norm them to the Dirac δ function. The first ionization threshold is described by $f^+ \equiv (1s^2_{1/2}2s_{1/2})^e_{1/2}$ or $1s^2 2s\,^2S^e_{1/2}$ in LSJ notation. This first ionization potential is referred to as E^+ for the remainder of this work and its value is given by

$$E^+ = E\left(1s^2 2s\,^2S^e_{1/2}\right) - E\left(1s^2 2snp\,^1P^o_1\right), \tag{7}$$

depending on which excited $1s^2 2snp\,^1P^o_1$ level is studied. When higher ionization potentials are involved, such as $1s^2 2p\,^2P^o_{1/2}$ or $^2P^o_{3/2}$, the $\mathcal{F}^+$ denotation is used instead of f^+. The energy levels, bound-bound and bound-free dipole matrix elements, and autoionization rates have been computed using FAC. The discrete-continuum configuration interaction is described within the Fano model [61]

$$\langle r|H_0|r'\rangle = E_r\delta_{rr'}, \tag{8}$$

$$\langle r|H_0|f^+,\epsilon\kappa;J^\pi\rangle = V_{r,J\kappa}(\epsilon)\delta_{JJ_r}\delta_{\pi\pi_r}, \tag{9}$$

$$\begin{aligned}&\langle f^+,\epsilon\kappa;J^\pi|H_0|f^+,\epsilon'\kappa';J'^{\pi'}\rangle \\ &\quad = (E^+ + \epsilon)\delta(\epsilon-\epsilon')\delta_{\kappa\kappa'}\delta_{JJ'}\delta_{\pi\pi'},\end{aligned} \tag{10}$$

where r is a resonance of $J_r^{\pi_r}$ symmetry with energy E_r and $V_{r,J\kappa}(\epsilon)$ is a partial autoionization amplitude of resonance r into a coupled target-continuum state $|f^+,\epsilon\kappa;J^\pi\rangle$. For simplicity, the excited state $1s^2 2snp\,^1P^o_1$ is denoted by $|1^o\rangle$. The electric dipole matrix elements between the excited state and a quasibound $|r^e\rangle$ level or an open channel $|f^+,\epsilon\kappa;J^\pi\rangle$ is denoted by $z_{1,r}$ or $z_{1,J\kappa}(\epsilon)$, respectively. Transition probabilities are also computed between discrete energy levels [58]

$$A_{ij} = \frac{2\alpha^3\omega_{ij}^3}{3g_j}|\langle j||\hat{z}||i\rangle|^2, \tag{11}$$

where i and f are initial and final levels, $\omega_{ij} = E_i - E_j$ is the energy level difference, g_j is the weight of the final state, $\langle j||\hat{z}||i\rangle$ is the electric dipole reduced matrix element, and α is the fine-structure constant.

B. Time-dependent Dirac equation

The general Dirac Hamiltonian contains a stationary $\hat{H}_0$ component describing the atomic system as mentioned in the preceding section and a time-dependent potential $\hat{H}_{\rm int}(t)$ representing the interaction of an external laser field with the given atomic system:

$$\hat{H}(t) = \hat{H}_0 + \hat{H}_{\rm int}(t). \tag{12}$$

The time-dependent interaction in the length gauge is given by $\hat{H}_{\rm int}(t) = \hat{z}E(t)$. The electric field of a linearly polarized laser beam tuned to a frequency ω is written in the slowly varying envelope approximation as

$$E(t) = \tfrac{1}{2}[\mathcal{E}(t)e^{-i\omega t} + \mathcal{E}^*(t)e^{i\omega t}]. \tag{13}$$

The electric-field envelope is a Gaussian function of time and is related to the cycled averaged laser intensity

$$I(t) = \frac{|\mathcal{E}(t)|^2}{8\pi\alpha}. \tag{14}$$

The evolution of the atomic system subjected to laser-field interaction is described by the time-dependent Dirac equation in the Schrödinger picture

$$i\frac{\partial|\Psi,t\rangle}{\partial t} = H(t)|\Psi,t\rangle. \tag{15}$$

The direct and resonant photoionizations within the vicinity of first ionization threshold are treated separately in the following sections. For all intended purposes, it is assumed that

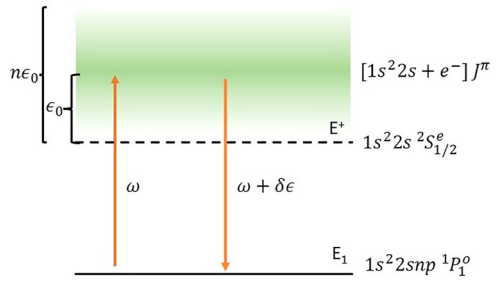

FIG. 1. Nonresonant photoionization of $1s^2 2snp\,^1P^o_1$ (first arrow) and stimulated radiative recombination on the $1s^2 2s\,^2S^e_{1/2}$ target ion (second arrow) driven by a pulsed laser field of frequency $\omega > E^+$.

the field-ion interaction starts at $t = 0$ and is maintained over the laser pulse duration.

C. Nonresonant photoionization

The field-induced dynamics between a bound state $1s^2 2snp\,^1P^o_1$ labeled as $|1^o\rangle$ and the degenerate open channels $|f^+, \epsilon\kappa; J^e\rangle$ of energy $E^+ + \epsilon$ is investigated in the absence of autoionization levels as shown schematically in Fig. 1. The system wave function is

$$|\Psi, t\rangle = c_1(t)e^{-iE_1 t}|1^o\rangle + \sum_{J,\kappa}\int_0^{n\epsilon_0} g_{J\kappa}(\epsilon, t)e^{-i(E^+ + \epsilon)t}|f^+, \epsilon\kappa; J^e\rangle d\epsilon. \quad (16)$$

The photoelectron energy is centered at $\epsilon_0 = E_1 + \omega - E^+$ and spans the domain from zero, corresponding to the ionization threshold, to a high enough energy value parametrized as $n\epsilon_0$, which captures the entire electron spectral distribution during the field-ion interactions, where n is a positive real number to be determined later by trial and error in accommodating the populations of continuum states. Solving the time-dependent Dirac equation gives

$$i\dot{c}_1(t) = \sum_{J,\kappa} z_{1,J\kappa}\frac{\mathcal{E}^*(t)}{2}\int_0^{n\epsilon_0} g_{J\kappa}(\epsilon, t)e^{-i(\epsilon-\epsilon_0)t}d\epsilon, \quad (17)$$

$$i\dot{g}_{J,\kappa}(\epsilon, t) = c_1(t)z_{J\kappa,1}\frac{\mathcal{E}(t)}{2}e^{i(\epsilon-\epsilon_0)t}. \quad (18)$$

The bound-free interaction terms have been evaluated at ϵ_0 and, since the energy dependence is shown to be smooth, these $z_{1,J\kappa}(\epsilon) \cong z_{1,J\kappa}(\epsilon_0)$ values are maintained throughout the calculation. As a result, the energy dependence has been dropped and the electric dipole elements have been pulled outside the energy integral. By performing the formal time integration of evolution equations corresponding to open channels, one obtains

$$g_{J\kappa}(\epsilon, t) = -i\int_{-\infty}^{t} z_{J\kappa,1}\frac{\mathcal{E}(t')}{2}c_1(t')e^{i(\epsilon-\epsilon_0)t'}dt'. \quad (19)$$

Substituting these expansion coefficients into the equation describing the evolution of the excited state and performing analytical integration leads to

$$\dot{c}_1(t) = -\frac{1}{4}S_{bf}\mathcal{E}^*(t)\int_{-\infty}^{t} c_1(t')\mathcal{E}(t')K(t-t')dt', \quad (20)$$

where S_{bf} is given by

$$S_{bf} = \sum_{J,\kappa}|z_{J\kappa,1}|^2 \quad (21)$$

and $K(t-t')$ is a nonlocal temporal kernel

$$K(t-t') = \frac{\sin[\epsilon_0(t-t')] + \sin[(n-1)\epsilon_0(t-t')]}{t-t'} - i\frac{\cos[\epsilon_0(t-t')] - \cos[(n-1)\epsilon_0(t-t')]}{t-t'}. \quad (22)$$

This approach completely decouples the evolution of discrete states from that of continuum states. Appendix A describes the behavior of this kernel and also provides evolution equations in the particular case of $\epsilon_0 \to \infty$ implemented within the local approximation:

$$\dot{c}_1(t) = -\frac{\Gamma_{ph}(t)}{2}c_1(t). \quad (23)$$

The term on the right-hand side constitutes a phenomenological decay rate for the photoionization process,

$$\Gamma_{ph}(t) = 2\pi\sum_{J,\kappa}\left|z_{J\kappa,1}\frac{\mathcal{E}(t)}{2}\right|^2 = \frac{1}{2}\pi S_{bf}|\mathcal{E}(t)|^2, \quad (24)$$

which is related to the spectral width of emitted photoelectrons. The local approximation cannot account for a finite ϵ_0, thus neglecting any threshold-related effects.

The time-dependent expansion coefficient corresponding to the excited level is obtained by numerically solving the integro-differential equation (20) via time discretization. Local approximation results are also provided by solving Eq. (23) instead. For each case the time- and energy-dependent coefficients corresponding to even-parity open channels are then determined using Eq. (18). Regardless of treatment, the total ion density should be a constant of motion, a feature expressed by the normalization condition

$$|c_1(t)|^2 + \sum_{J,\kappa}\int_0^{n\epsilon_0}|g_{J\kappa}(\epsilon, t)|^2 d\epsilon = 1. \quad (25)$$

Here the first term is the density of C^{2+} excited ions, while the second term simultaneously gives the electron yield and the density of C^{3+} ions.

The spectral distribution of emitted photoelectrons is obtained by summing the squared modulus of expansion coefficients corresponding to open states, for all possible partial symmetries, at the end of the interaction:

$$P(\epsilon) = \lim_{t\to\infty}\sum_{J,\kappa}|g_{J\kappa}(\epsilon, t)|^2. \quad (26)$$

Enforcing the local approximation when taking the limit $\epsilon_0 \to \infty$ automatically leads to a symmetric spectral distribution by virtue of Eq. (18), provided no fluctuations in the normal laser field are considered. In contrast, imposing a cutoff in the energy domain of photoelectrons corresponding to the forbidden threshold enhances nonlocal time contributions in the field-ion dynamics. In order to highlight the influence of threshold effects, results provided by both local and nonlocal approaches are presented in this work.

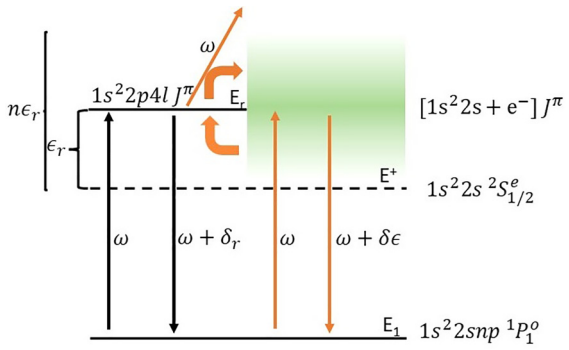

FIG. 2. Photoionization driven by a pulsed laser field of frequency ω tuned to the $1s^2 2p4l\ J^\pi$–$1s^2 2snp\ ^1P^o_1$ transition. The photoexcitation (first arrow) and stimulated emission of radiation (second arrow) are processes relating two discrete levels, while autoionization (bent orange arrows), direct photoionization (third arrow) and stimulated radiative recombination (fourth arrow) are discrete-continuum process.

D. Photoionization near a resonant state

In addition to direct channels, this section includes the interplay between photoexcitation from the $1s^2 2snp\ ^1P^o_1$ state labeled as $|1^o\rangle$ to an autoionization state of type $1s^2 2p4l\ J^\pi = 0, 1, 2^e$ of energy E_r expressed shortly by $|r^e\rangle$ and the subsequent stabilization processes (see Fig. 2). These refer to stimulated emission of radiation, autoionization, and photoionization from the quasibound state. In order to model the latter process, the configuration space is augmented with a new set of open channels with odd parity formed by excited C^{3+} target states coupled with a free electron. For all intended purposes it is considered that the laser frequency is tuned to the resonance energy such that $E_1 + \omega = E_r + \delta_r$, where δ_r is a considerably small detuning, and thus Auger electrons have energies around the $\epsilon_r = E_r - E^+ = \epsilon_0 - \delta_r$ value. The system wave function is given by

$$
\begin{aligned}
|\Psi, t\rangle = {} & c_1(t) e^{-iE_1 t} |1^o\rangle + d_r(t) e^{-iE_r t} |r^e\rangle \\
& + \sum_{J,\kappa} \int_0^{n\epsilon_r} g_{J\kappa}(\epsilon, t) e^{-i(E^+ + \epsilon)t} |f^+, \epsilon\kappa; J^e\rangle d\epsilon \\
& + \sum_{\mathcal{F},\mathcal{J},\mathcal{K}} \int_0^{2(\varepsilon_0 - \Delta^+_{\mathcal{F}})} h_{\mathcal{F}\mathcal{J}\mathcal{K}}(\varepsilon_{\mathcal{F}}, t) \\
& \times e^{-i(E^+_{\mathcal{F}} + \varepsilon_{\mathcal{F}})t} |\mathcal{F}^+, \varepsilon_{\mathcal{F}}\mathcal{K}; \mathcal{J}^o\rangle d\varepsilon_{\mathcal{F}},
\end{aligned} \tag{27}
$$

where $|\mathcal{F}^+, \varepsilon_{\mathcal{F}}\mathcal{K}, \mathcal{J}^o\rangle$ is an open channel of odd parity and total angular momentum $\mathcal{J}$, situated around $\varepsilon_0 = \epsilon_r + \omega$, and $h_{\mathcal{F}\mathcal{J}\mathcal{K}}(\varepsilon, t)$ is its corresponding expansion coefficient. These open channels are obtained by coupling a C^{3+} target of energy $E^+_{\mathcal{F}}$, i.e., $1s^2 2s\ ^2S^e_{1/2}$ and $1s^2 2p\ ^2P^o_{1/2;3/2}$, with a corresponding free electron of relativistic angular quantum number $\mathcal{K}$ and energy $\varepsilon_{\mathcal{F}}$. Since the photoelectron energy domain starts from their respective threshold, the upper limit of the energy integral for odd-parity open channels is given by $\varepsilon_0 - \Delta^+_{\mathcal{F}}$, where $\Delta^+_{\mathcal{F}} = E^+_{\mathcal{F}} - E^+$ is the energy of higher ionization thresholds relative to the first one. The derivation of evolution equations for discrete and continuum states given by the time-dependent Dirac equation is presented in Appendix B. The discrete-state evolution equations are given by

$$
\begin{aligned}
\dot{c}_1(t) = {} & -i d_r(t) e^{i\delta_r t} z_{1,r} \frac{\mathcal{E}^*(t)}{2} \\
& - \frac{1}{4} S_{bf} \mathcal{E}^*(t) \int_{-\infty}^{t} c_1(t') \mathcal{E}(t') e^{i\delta_r (t - t')} K(t - t') dt' \\
& - \frac{1}{2} I^*_{br} \mathcal{E}^*(t) e^{i\delta_r t} \int_{-\infty}^{t} d_r(t') K(t - t') dt',
\end{aligned} \tag{28}
$$

$$
\begin{aligned}
\dot{d}_r(t) = {} & -i c_1(t) e^{-i\delta_r t} z_{r,1} \frac{\mathcal{E}(t)}{2} - \frac{\Gamma_{sph}(t)}{2} d_r(t) \\
& - \frac{\Gamma_r}{2\pi} \int_{-\infty}^{t} d_r(t') K(t - t') dt' \\
& - \frac{1}{2} I_{br} \int_{-\infty}^{t} c_1(t') e^{i\delta_r t'} \mathcal{E}(t') K(t - t') dt',
\end{aligned} \tag{29}
$$

with S_{bf} and $K(t - t')$ previously defined in Eqs. (21) and (22). The interference term I_{br} between direct and resonant channels is given by

$$
I_{br} = \sum_{J,\kappa} V_{r,J\kappa} z_{J\kappa,1} \delta_{JJ_r}. \tag{30}
$$

The phenomenological decay rates for secondary photoionization and autoionization are given by

$$
\Gamma_{sph}(t) = 2\pi \sum_{\mathcal{F},\mathcal{J},\mathcal{K}} \left| z_{\mathcal{F}\mathcal{J}\mathcal{K},r} \frac{\mathcal{E}(t)}{2} \right|^2, \tag{31}
$$

$$
\Gamma_r = 2\pi \sum_{J,\kappa} |V_{J\kappa,r}|^2 \delta_{JJ_r} = 2\pi \sum_{\kappa} |V_{J_r\kappa,r}|^2. \tag{32}
$$

The first term on the right-hand side of Eq. (28) represents the field-driven interaction between the bound level $|1^o\rangle$ and resonance $|r^e\rangle$, manifesting as photoexcitation or stimulated emission of radiation. The second term provides the rate of change for $c_1(t)$ after the field-driven bound-free interaction consisting in photoionization and stimulated radiative recombination. The last term describes the interference between direct and resonant channels comprising autoionization of the quasibound state $|r^e\rangle$ followed by stimulated radiative recombination.

Similarly, the first term on the right-hand side of Eq. (29) represents the field-driven interaction between bound and autoionizing levels, showcasing the photoexcitation-stimulated emission interplay. The second term couples the resonance state $|r^e\rangle$ with odd-parity continuum states through the driving field. The third term describes autoionization of the quasibound state $|r^e\rangle$ while also allowing its inverse process, dielectronic capture, to occur. The last term expresses the interference between direct and resonant channels, in the form of photoionization of $|1^o\rangle$ followed by dielectronic capture onto the resonant state $|r^e\rangle$.

The free states of even and odd parity are governed by the following equations, respectively, as given by solving the time-dependent Dirac equation:

$$
\begin{aligned}
i\dot{g}_{J\kappa}(\epsilon, t) = {} & c_1(t) z_{J\kappa,1} \frac{\mathcal{E}(t)}{2} e^{i(\epsilon - \epsilon_0)t} \\
& + d_r(t) V_{J\kappa,r} e^{i(\epsilon - \epsilon_0 + \delta_r)t} \delta_{JJ_r},
\end{aligned} \tag{33}
$$

$$
i\dot{h}_{\mathcal{F}\mathcal{J}\mathcal{K}}(\varepsilon_{\mathcal{F}}, t) = d_r(t) z_{\mathcal{F}\mathcal{J}\mathcal{K},r} \frac{\mathcal{E}(t)}{2} e^{i(\varepsilon_{\mathcal{F}} - \varepsilon_0 + \Delta^+_{\mathcal{F}})t}. \tag{34}
$$

The coupled integro-differential equations (28) and (29) are solved self-consistently by time discretization for different increasing n values. Once the solutions converge, Eqs. (33) and (34) are used to compute the expansion coefficients corresponding to even and odd open channels, respectively. Accommodation of electrons to different free states without abrupt cutoffs occurring at the higher end of the spectrum is further verified along with the conservation of the system norm.

In order to obtain the solutions within the local approximation, one must take the $\epsilon_r \to \infty$ limit. Evolution equations for discrete states are then simplified to

$$\dot{c}_1(t) = -id_r(t)e^{i\delta_r t}z_{1,r}\frac{\mathcal{E}^*(t)}{2} - \frac{\pi}{2}I^*_{br}\mathcal{E}^*(t)d_r(t)e^{i\delta_r t} - \frac{\Gamma_{ph}(t)}{2}c_1(t), \quad (35)$$

$$\dot{d}_r(t) = -ic_1(t)e^{-i\delta_r t}z_{r,1}\frac{\mathcal{E}(t)}{2} - \frac{\pi}{2}I_{br}\mathcal{E}(t)c_1(t)e^{i\delta_r t} - \frac{\Gamma_{sph}(t)+\Gamma_r}{2}d_r(t). \quad (36)$$

The coupled equations (35) and (36) are solved numerically and their solutions are used to determine the free states using Eqs. (33) and (34). Whether the treatment allows for nonlocal contributions or not, the system is closed, so the total ion density is constant at all times:

$$|c_1(t)|^2 + |d_r(t)|^2 + \sum_{J,\kappa}\int_0^{n\epsilon_r}|g_{J\kappa}(\epsilon,t)|^2 d\epsilon + \sum_{\mathcal{F},\mathcal{J},\mathcal{K}}\int_0^{2(\varepsilon_0-\Delta^+_{\mathcal{F}})}|h_{\mathcal{F}\mathcal{J}\mathcal{K}}(\varepsilon_{\mathcal{F}},t)|^2 d\varepsilon_{\mathcal{F}} = 1. \quad (37)$$

The spectral distributions for the emitted electrons at the end of the field-ion interaction are given by

$$P_{\text{ph+Auger}}(\epsilon) = \lim_{t\to\infty}\sum_{J,\kappa}|g_{J\kappa}(\epsilon,t)|^2, \quad (38)$$

$$P_{sph}(\varepsilon) = \lim_{t\to\infty}\sum_{\mathcal{F},\mathcal{J},\mathcal{K}}|h_{\mathcal{F}\mathcal{J}\mathcal{K}}(\varepsilon-\Delta^+_{\mathcal{F}},t)|^2. \quad (39)$$

Due to interference between direct and resonant channels, the Auger electrons and photoelectrons are distributed around ϵ_r and ϵ_0. These two values coincide when detuning is set to zero.

III. STRUCTURE CALCULATIONS

The relativistic single-particle orbitals are determined by simultaneously optimizing the $1s^22s^2$ (20%), $1s^22s2p$ (40%), $1s^22p4p$ (20%), and $1s^22p4f$ (20%) configurations (nonrelativistic notation) relevant for the photoionization process. This is performed through the Dirac-Fock-Slater iteration on the fictitious mean configuration $1s^2_{1/2}2s^{0.8}_{1/2}2p^{0.267}_{1/2}2p^{0.533}_{3/2}4p^{0.067}_{1/2}4p^{0.133}_{3/2}4f^{0.086}_{5/2}4f^{0.114}_{7/2}$. The electrostatic potential based on this fictitious mean configuration is also used to compute the free-electron orbitals within the distorted-wave approximation. Individual CSFs corresponding to the fine-structure levels presented in Scheme 1 and Table I have been constructed using the optimized relativistic single-particle orbitals. In order to account for correlation [62], the configuration space has been augmented with additional CSFs arising from $1s^22ln'l'$, with $l \leqslant 1$, $n' \leqslant 7$, and $l' \leqslant 6$, and $1s^23ln'l'$, with $l \leqslant 2$, $n' \leqslant 5$, and $l' \leqslant 4$. Supplementary CSFs of 0^e symmetry arising from $1s^2nln'l'$, with $n \leqslant 5$, $l < n$, $n' \leqslant 7$, and $l' < n'$, have been included in order to lower the energy of the $1s^22p4p\,^1S^e_0$ level.

TABLE II. Transition energies (eV) and probabilities (s^{-1}) for $1s^22s^2\,^1S^e_0$–$1s^22snp\,^1P^o_1$ ($n \leqslant 5$) compared to the NIST data [57].

Excited state	Transition energy (eV)		Transition probability (s^{-1})	
	Present	NIST	Present	NIST
$2s2p\,^1P^o_1$	13.44319	12.690036	2.069×10^9	1.769×10^9
$2s3p\,^1P^o_1$	32.05170	32.103388	3.467×10^9	3.460×10^9
$2s4p\,^1P^o_1$	40.17330	39.973026	6.045×10^8	6.560×10^8
$2s5p\,^1P^o_1$	42.52235	42.558572	1.960×10^9	1.180×10^9

The mean configuration has been chosen in order to minimize deviations from experimental results, such as resonance positions, autoionization rates, and to a lesser extent the first excited levels of C^{2+}. This is reflected in the transition energies and probabilities shown in Table II, where the $1s^22s2p\,^1P^o_1$ level has an absolute deviation of roughly 0.75 eV. However, for higher levels with $n = 3, 4, 5$, the absolute deviations are 0.05, 0.2, and 0.04 eV, respectively. These translate into relative errors of 5.9%, 0.1%, 0.5%, and 0.1% for $n = 2, 3, 4, 5$, respectively. The radiative transition probabilities agree to within 17%, 0.2%, 7%, and 66% for the excited levels corresponding to $n = 2, 3, 4, 5$, respectively. Electric dipole matrix elements for bound-free transitions calculated at $\epsilon_0 = 0.1$ and 0.485 eV photoelectron energies are shown in Table III. Figure 3 also shows the dependence of bound-free electric dipole matrix elements on photoelectron energy above the first ionization threshold, within the $\epsilon \in [0.01, 5\text{ eV}]$ domain, between each excited $1s^22snp\,^1P^o_1$ state, with $n \leqslant 5$, and all degenerate channels of even parity. The variation with energy is smooth enough, with few exceptions in the case of the $1s^22s4p\,^1P^o_1$ state, to consider the dipole elements as constants around a central photoelectron energy value. In the case of resonance positions and widths, comparisons are provided with the measured values of Mannervik *et al.* [28] and the theoretical MBPT CI results of Derevianko *et al.* [30] in Table IV. Good overall agreement is reached between the present results and the values from the mentioned works.

In the case of the $1s^22p4f\,^3F^e_2$ level, the present energy is 15 meV higher than the measured value. The highest deviation in width is given by the $1s^22p4f\,^1D^e_2$ level, where the present calculations underestimate the measured value by 36%, whereas the MBPT CI approach overestimates the experimental value by a factor 3. This indicates that the present atomic model is suitable to further compute autoionization amplitudes and bound-(quasi)bound transitions necessary for the time-dependent calculations. Table V gives the electric dipole matrix elements between bound $1s^22snp\,^1P^o_1$ and autoionization $1s^22pnl$ levels, respectively, with $n \leqslant 5$ and $l = 1, 3$.

Except for $2s2p$-$2p4p$ and $2s4p$-$2p4p$ transitions, most combinations are nonzero only due to configuration mixing.

TABLE III. Bound-free electric dipole matrix elements in atomic units $ea_0/\sqrt{E_H}$. Results are provided for open channels of 0.1 and 0.485 eV energy above the first ionization threshold, respectively. The corresponding photon energy ω and photoelectron energy ϵ_0 are also provided.

Bound state	LSJ notation	Photon energy (eV)	Photoelectron energy (eV)	Open channels				
				$(2s_{1/2}\epsilon s_{1/2})^e_0$	$(2s_{1/2}\epsilon s_{1/2})^e_1$	$(2s_{1/2}\epsilon d_{3/2})^e_1$	$(2s_{1/2}\epsilon d_{3/2})^e_2$	$(2s_{1/2}\epsilon d_{5/2})^e_2$
$(2s_{1/2}2p_{3/2})^o_1$	$2s2p\,^1P^o_1$	35.683	0.485	−0.0271	0.0756	0.4209	0.3758	0.6928
		35.298	0.1	−0.0205	0.0567	0.4099	0.3659	0.6747
$(2s_{1/2}3p_{3/2})^o_1$	$2s3p\,^1P^o_1$	16.269	0.485	−0.1901	0.5786	1.0545	0.9772	1.6912
		15.884	0.1	−0.1890	0.5754	1.0685	0.9901	1.7137
$(2s_{1/2}4p_{3/2})^o_1$	$2s4p\,^1P^o_1$	8.400	0.485	−0.0084	0.0215	0.3983	0.3552	0.6569
		8.015	0.1	0.0287	−0.0835	0.3256	0.2902	0.5364
$(2s_{1/2}5p_{3/2})^o_1$	$2s5p\,^1P^o_1$	5.814	0.485	−0.6967	1.9186	2.3118	2.0404	3.8322
		5.429	0.1	−0.7544	2.0772	2.4813	2.1897	4.1134

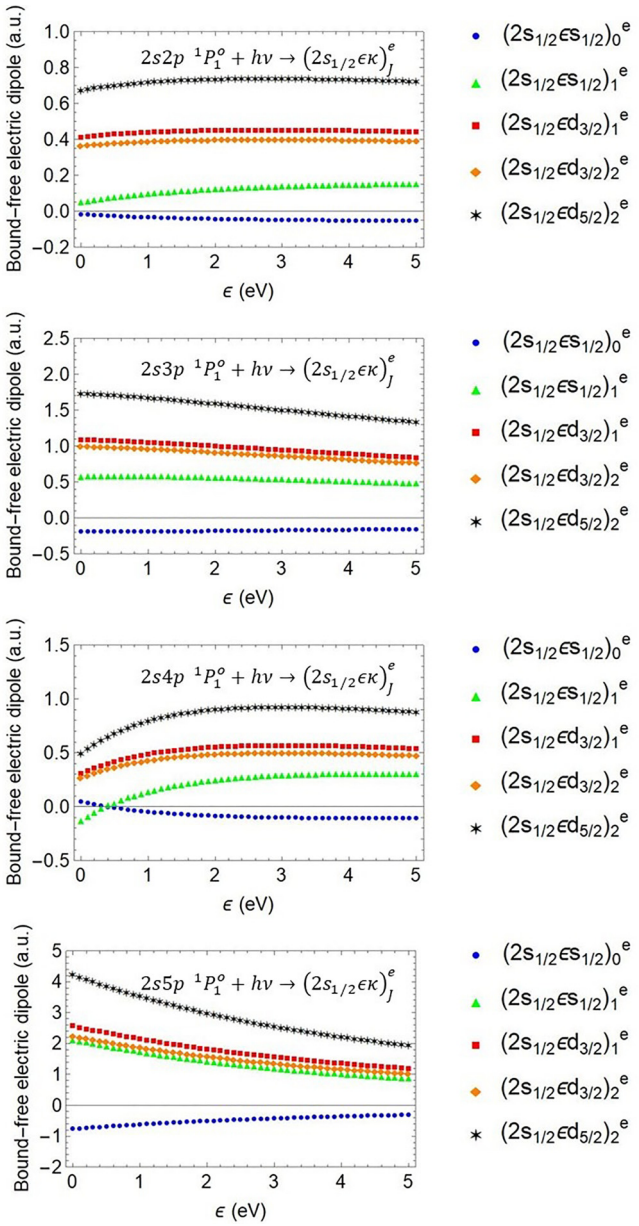

FIG. 3. Bound-free electric dipole matrix elements between $1s^2 2snp\,^1P^o_1$ levels ($n \leqslant 5$) and $(1s^2_{1/2}2s_{1/2}\epsilon\kappa)^e_J$ open channels of [0.01, 5 eV] energy above the first ionization threshold.

The cutoff has been set at 10^{-4} such that CSFs contributions to a certain level that do not exceed this value are simply neglected. As a result, some states cannot couple through an electric dipole transition even via configuration mixing. The missing values from Table V correspond to weak transitions between such states. Significantly more configurations need to be included together with a much lower cutoff in order to estimate the values for these transitions which are beyond the scope of this work.

Finally, in order to account for the photoionization of quasibound states, it is necessary to compute a secondary set of open channels with odd parity for certain continuum energies. The (quasi)bound-free transitions are readily determined by FAC. This type of transition comprises a damping source for the resonant Auger effect. The selection rules allow for the population of seven odd open channels as described by Table VI.

IV. RESULTS AND DISCUSSION

A. Threshold effects on nonresonant photoionization

The results corresponding to nonresonant or direct photoionization of the $1s^2 2s2p\,^1P^o_1$ level belonging to C^{2+}, barely above the threshold at $\epsilon_0 = 0.1$ eV, are presented in this section. Numerical calculations have been done based on Eqs. (18) and (20) by discretizing the time domain into 10^6 equal steps. The timescale of photoelectrons near $\epsilon_0 = 0.1$ eV is about $\tau = 2\pi/\epsilon_0 \sim 41.33$ fs. For this reason, three pulses of 20, 40, and 80 fs FWHM values are included in the calculations presented in Figs. 4 and 5. Results obtained within the local approximation based on Eqs. (18) and (23) are provided as open symbols linked by dashed lines for comparison. The ionization dynamics is severely altered for laser pulse duration below the photoelectron timescale, as can be seen in Fig. 4. The laser field continues to act upon the newly formed C^{3+} ions in their ground state and slow electrons after the initial photoionization, leading to highly nonlinear phenomena. At low photoelectron energies, the laser-stimulated radiative recombination of electrons with nearby ions is enabled, thus suppressing the overall ionization of the system, as can be seen in Figs. 4 and 5. Given that the stimulated recombination is the inverse process of pulsed photoionization, both occurring within the same field, it is more likely for the electrons

TABLE IV. Resonance positions and widths. The values are taken from the present Dirac-Fock-Slater approach within the distorted-wave approximation, ion storage ring measurements carried out by Mannervik *et al.* [28], and theoretical MBPT CI calculations performed by Derevianko *et al.* [30].

Quasibound state	LSJ notation	Position (eV)			Width (meV)		
		Expt. [28]	Present	MBPT CI [30]	Expt. [28]	Present	MBPT CI [30]
$(2p_{1/2}4f_{5/2})^e_2$	$2p4f\,^3F^e_2$	0.240	0.255	0.242	10^{-3}	0.73×10^{-3}	50×10^{-3}
$(2p_{3/2}4f_{5/2})^e_2$	$2p4f\,^3D^e_2$	0.430	0.430	0.431	1.01	0.95	1.10
$(2p_{3/2}4f_{5/2})^e_1$	$2p4f\,^3D^e_1$	0.433	0.433	0.435	1.01	0.97	1.10
$(2p_{3/2}4f_{7/2})^e_2$	$2p4f\,^1D^e_2$	0.452	0.451	0.451	0.22	0.14	0.60
$(2p_{3/2}4p_{3/2})^e_0$	$2p4p\,^1S^e_0$	0.485	0.477	0.451	221	252	202

to recombine with newly formed C^{3+} targets obtaining previously excited C^{2+} ions. This is shown schematically as

$$C^{3+} + e^- + h\nu \rightarrow \begin{cases} (C^{2+})^* + 2h\nu & \text{(laser-stimulated radiative recombination)} \\ (C^{3+} + e^-)^* & \text{(photoabsorption)}, \end{cases} \tag{40}$$

which refers to the laser-stimulated radiative recombination and above-threshold photoabsorption by the C^{3+} ion target coupled with the free electron. Pulsed photoionization and stimulated radiative recombination cycles are observed in the field-ion dynamics, essentially representing Rabi oscillations between a bound and a free state of this quantum system. The photoabsorption constitutes a competing process for the stimulated radiative recombination, thus becoming one of the main damping sources for the bound-free Rabi oscillations. Further single-photon ionization of C^{3+} target ions is excluded since the photon energies shown in Table III are below the 64.493 52-eV threshold value given by NIST [57]. Instead, the photoabsorption process includes all possible allowed combinations of C^{3+} photoexcitation and free-electron inverse bremsstrahlung to form an open channel of 35.398 eV energy and odd parity. Configuration-interaction effects on the open channels would further mix all CSFs formed by coupling a C^{3+} target, such as $1s^22s\,^2S^e_{1/2}$ and $1s^22p\,^2P^o_{1/2,3/2}$, with a free electron matching the required energy difference while respecting parity conservation and the triangle condition for angular momentum addition. Free-free transitions are not computed in this work; thus they are not accounted for in the ionization dynamics. A simple atomic physics explanation is provided as justification for neglecting the photoabsorption process. The asymptotic form for the photoelectron (large-component) wave function [63] is proportional to approximately $\sin\{k(\epsilon)r + \frac{Z_{\text{eff}}}{k(\epsilon)}\ln[2k(\epsilon)r] - \frac{1}{2}\kappa\pi + \delta_\kappa\}$, where $k(\epsilon) \approx \sqrt{2\epsilon}$ is the photoelectron momentum, Z_{eff} is the effective charge of the target ion, and δ_κ is a phase depending on the relativistic angular quantum number. When computing bound-free transitions for low photoelectron energies, the free-particle wave function executes fewer spatial oscillations within the overlapping space with the discrete localized bound state. In contrast, at high free electron energies, more spatial oscillations occur in the same space such that slowly varying neighboring contributions corresponding to the discrete function start canceling each other, significantly reducing the bound-free interaction terms. This is consistent with the quasirelativistic asymptotic scaling law for bound-free transitions with a free-particle energy of approximately $\epsilon^{-5/3}$ [64,65]. In a similar fashion, purely electric dipole free-free transitions decrease rapidly with increasing energy difference between the two states ω as shown in the quasiclassical scaling $\omega^{-5/3}$ occurring when the two states do not have comparable energies [64,65], i.e., 0.1 eV versus 35.398 eV. These energy scaling laws have two main consequences on the direct photoionization of the $1s^22s2p\,^1P^o_1$ state near the first threshold. The bound-free transitions become exceedingly high at this photoelectron energy range, while free-free transitions between states of energies 0.1 and 35.398 eV become less relevant for the overall process.

TABLE V. Bound-(quasi)bound electric dipole matrix elements between $1s^22snp\,^1P^o_1$ levels ($n \leqslant 5$) and $1s^22p4l$ ($l = 1, 3$) autoionization states in atomic units ea_0.

Quasibound states	Bound states			
	$2s2p\,^1P^o_1$	$2s3p\,^1P^o_1$	$2s4p\,^1P^o_1$	$2s5p\,^1P^o_1$
$2p4f\,^3F^e_2$	-3.015×10^{-3}	-1.215×10^{-2}	-4.586×10^{-3}	-6.316×10^{-2}
$2p4f\,^3D^e_2$		8.645×10^{-2}	3.576×10^{-2}	3.247
$2p4f\,^3D^e_1$		6.355×10^{-3}		1.906
$2p4f\,^1D^e_2$	1.209×10^{-2}	-4.582×10^{-1}	-2.067×10^{-1}	5.325×10^{-1}
$2p4p\,^1S^e_0$	-9.187×10^{-2}	9.038×10^{-3}	2.090×10^{-1}	

TABLE VI. (Quasi)bound-free electric dipole matrix elements in atomic units $ea_0/\sqrt{E_H}$ between the autoionizing $1s^2 2p4p\,{}^1S_0^e$ level and the $(1s^2_{1/2}2s_{1/2}\varepsilon\mathcal{K})^o_{\mathcal{J}}$, $(1s^2_{1/2}2p_{1/2}\varepsilon\mathcal{K})^o_{\mathcal{J}}$, and $(1s^2_{1/2}2p_{3/2}\varepsilon\mathcal{K})^o_{\mathcal{J}}$ odd open channels of 0.485 eV + ω energy.

Odd open channels	Photon energy (eV)			
	$\omega = 35.682$	$\omega = 16.269$	$\omega = 8.400$	$\omega = 5.814$
$(2s_{1/2}\varepsilon p_{1/2})^o_1$	−0.0701	−0.1443	−0.2311	−0.2842
$(2s_{1/2}\varepsilon p_{3/2})^o_1$	0.0991	0.2039	0.3266	0.4016
$(2p_{1/2}\varepsilon s_{1/2})^o_1$	0.0597	0.1421	0.2361	0.2856
$(2p_{1/2}\varepsilon d_{3/2})^o_1$	−0.1979	−0.4660	−0.7599	−0.9137
$(2p_{3/2}\varepsilon s_{1/2})^o_1$	0.0861	0.2058	0.3436	0.4168
$(2p_{3/2}\varepsilon d_{3/2})^o_1$	0.0902	0.2129	0.3483	0.4197
$(2p_{3/2}\varepsilon d_{5/2})^o_1$	−0.2705	−0.6389	−1.0451	−1.2593

The threshold effects have a simple physical explanation. For increasing field intensities the photoelectron spectral distribution broadens and, in the case of photoionization barely above a threshold, the low-energy tail of said distribution starts approaching the forbidden energy region, significantly affecting the ionization dynamics. This perspective gives two main requirements for obtaining bound-free Rabi oscillations. First, the timescale of photoelectrons needs to be comparable to or higher than that of the driving field, since slower electrons are more likely to further interact with the field via radiative recombination, contrary to fast electrons, which generally escape such processes. This can also be understood by the fact that a shorter laser pulse leads to a more broadened photoelectron distribution pushing into the forbidden energy region giving rise to enhanced threshold effects, while a longer laser pulse corresponds to a tighter electron spectral distribution, mitigating said effects. This can be emphasized in the density of excited C^{2+} ions presented in Fig. 4, where three laser pulses of different duration, namely, 20, 40, and 80 fs FWHM values, are used to photoionize the $1s^2 2s2p\,{}^1P_1^o$ state just 0.1 eV above the first ionization threshold for intensities ranging from 10^{10} to 10^{16} W/cm^2.

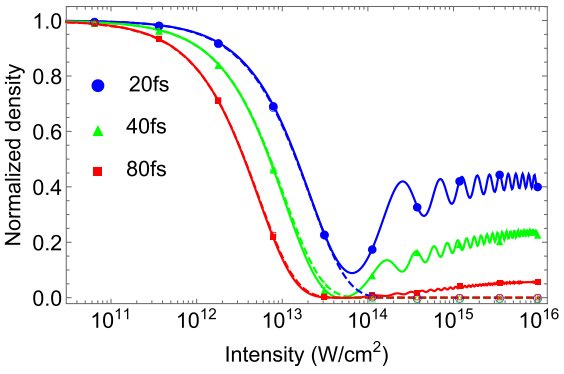

FIG. 4. Density of $1s^2 2s2p\,{}^1P_1^o$ excited C^{2+} ions after direct photoionization 0.1 eV above the first threshold using three laser pulses of 20 (blue circles), 40 (green triangles), and 80 (red squares) fs FWHM duration. Corresponding open symbols linked by dashed lines represent local approximation results obtained by solving Eq. (23).

At a 10^{16} W/cm^2 laser intensity, the stimulated recombination process leads to a electron yield reduction of up to 43%, 21%, and 5% for the 20, 40, and 80-fs pulses, respectively, compared to a local approximation approach. This clearly shows how photoionization suppression is enhanced for decreasing pulse duration, especially below the timescale of corresponding photoelectrons. Second, for higher laser intensity values the decay width $\Gamma_{ph}(t)$ from Eq. (24) becomes comparable to ϵ_0 such that one can use the relation (14) to roughly estimate the critical value (in atomic units)

$$I_{bf}^{th} = \frac{\epsilon_0}{8\pi^2\alpha\left(\sum_{J,\kappa}|z_{J\kappa,1}|^2\right)}. \tag{41}$$

These estimates only apply when the pulse duration is comparable to the photoelectron timescale $\tau \sim 2\pi/\epsilon_0$. At first glance the required intensity seems to depend linearly on the central photoelectron energy ϵ_0; however, one must account for the fact that bound-free electric dipole elements $z_{J\kappa,1}$ are evaluated at $\epsilon = \epsilon_0$. Near the ionization threshold, the bound-free electric dipole matrix elements oscillate with energy, imprinting this behavior on the intensity. Asymptotically, these values scale with approximately $\epsilon_0^{-5/3}$ such that the required intensity for bound-free Rabi oscillations rapidly increases with the central photoelectron energy as $I_{bf}^{th} \sim \epsilon_0^{13/3}$, making these effects unfeasible when photoionizing away from thresholds. This is emphasized in Table VII, which gives the minimal intensity values required for laser pulses of timescale comparable to that of the free electrons to induce threshold effects for $\epsilon_0 = 0.1$, 1, 10, and 100 eV central photoelectron energies.

The required intensity values for ionization suppression are highly dependent on temporal and frequency profiles of the laser pulse. A sinusoidal laser pulse would lead to a vastly different electron distribution compared to a Gaussian or step pulse according to the laws of Fourier transformation. A shorter (or larger) temporal duration would generally lead to a larger (or shorter) photoelectron energy width which in turn would correspond to lower (or higher) required intensities for the manifestation of threshold effects as shown in Fig. 4, where the breakdown point of the local approximation occurs at slightly different intensities around the 5.4×10^{13} W/cm^2 value presented in Table VII. Figure 5 (top row) shows the formation of Rabi oscillations in the density of photoelectrons over time starting from the laser intensity 2×10^{14} W/cm^2. In the case of laser pulses with 2×10^{15} W/cm^2 intensity, there are 4, 8, and 16 Rabi cycles occurring for the 20, 40, and 80 fs FWHM pulse durations, respectively. Surprisingly, the number of Rabi oscillations increases with pulse duration; however, their corresponding oscillation amplitudes rapidly decrease up to the point that they are no longer visible in the ion density or electron yield. It is worth mentioning that during the exponential decay stage of the photoionization process, local approximation results tend to deviate more for decreasing pulse durations, as seen in the top row of Fig. 5.

The spectral distribution of emitted electrons recorded at the end of the field-ion interaction is presented in the bottom row of Fig. 5 for the mentioned femtosecond pulses at three intensity values showcasing the breakdown of the local approximation. At the beginning of the interaction the

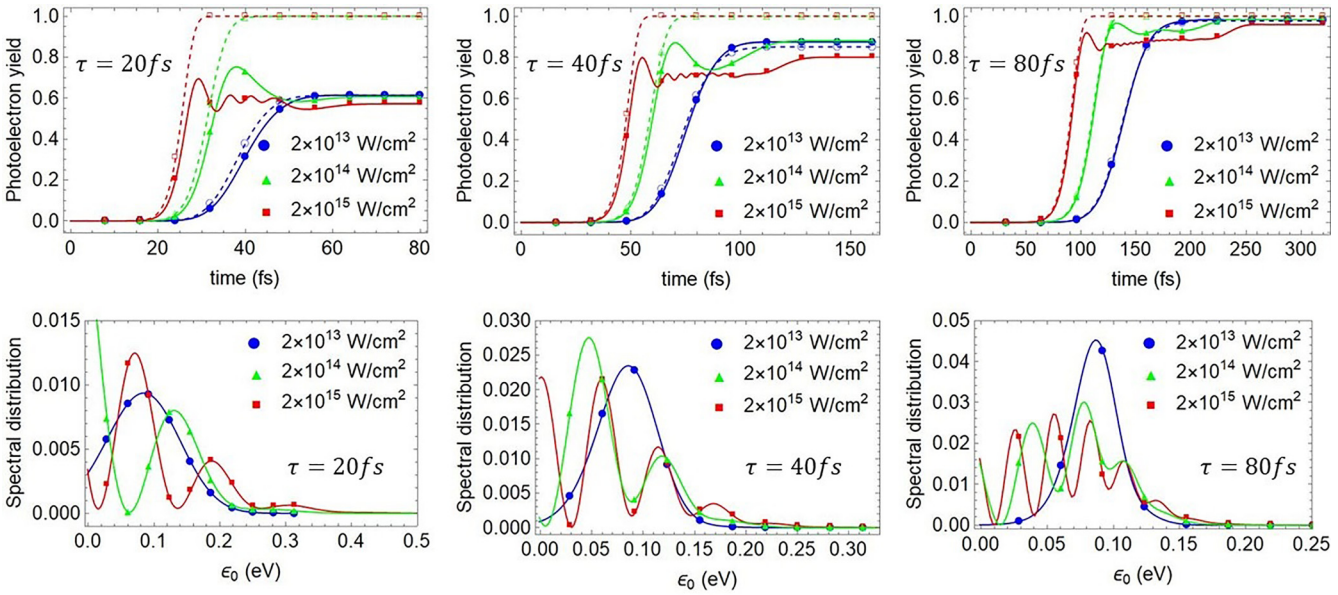

FIG. 5. Direct photoionization of the $1s^2 2s2p\,^1P_1^o$ level near ($\epsilon_0 = 0.1$ eV) the first ionization threshold of the C^{2+} ion. Photoelectron yield (top row) and spectral distribution (bottom row) are shown for a laser pulse duration of 20 fs (left column), 40 fs (middle column), and 80 fs (right column). The corresponding open symbols linked by dashed lines (top row) represent results obtained within the local approximation approach. Laser intensities have been chosen to showcase the breakdown of the local approximation together with the development of near-threshold effects.

spectral distribution of photoelectrons resembles a Lorentzian profile abruptly cut off near the threshold region and is further modulated, approaching a Gaussian shape at the end of the interaction, imprinted by the laser pulse profile. For higher intensities, near the first ionization threshold, these Gaussian forms are steadily redshifted while also being modulated by the ionization dynamics leading to the formation of multipeak structures as shown in the bottom row of Fig. 5. Despite the fact that spectral modulations appear together with the suppression of ionization, the former are much more sensitive to changes in driving field parameters. For example, in the case of a 80 fs FWHM pulse, at the end of the interaction, the electron yield only slightly deviates, up to 3%, from the local approximation results; however, the spectral distribution is completely different from that of the expected simple Gaussian or Lorentzian shape. These results essentially follow the formation of Rabi cycles, namely, the number of peaks increases with the duration of laser pulses, while the ratio between neighboring peaks decreases. The local minima within the spectral distribution increase for higher pulse durations up to the point where they approach the local maxima such that threshold effects become negligible.

TABLE VII. Required laser intensity values to produce bound-free Rabi oscillations in the photoionization of $1s^2 2snp\,^1P_1^o$ levels belonging to the C^{2+} ion for different central photoelectric energies ϵ_0 (eV). The necessary values for laser pulse duration (FWHM) are also presented.

	Intensity (W/cm^2)			
Excited state	$\epsilon_0 = 0.1$ $\tau \lessapprox 40$ fs	1 4 fs	10 400 as	100 40 as
$2s2p\,^1P_1^o$	5.4×10^{13}	4.8×10^{14}	5.8×10^{15}	2.2×10^{18}
$2s3p\,^1P_1^o$	7.6×10^{12}	7.9×10^{13}	2.3×10^{15}	3.9×10^{18}
$2s4p\,^1P_1^o$	8.8×10^{13}	3.9×10^{14}	5.1×10^{15}	1.1×10^{19}
$2s5p\,^1P_1^o$	1.3×10^{12}	1.7×10^{13}	1.8×10^{15}	1.0×10^{19}

B. Threshold effects on photoionization near a resonant state

The photoionization from the initial $1s^2 2s2p\,^1P_1^o$ state belonging to the C^{2+} ion by using a laser field tuned to the resonant $2s2p\,^1P_1^o$–$2p4p\,^1S_0^e$ transition, i.e., $\epsilon_0 = 0.485$ eV with the detuning set to zero $\delta_r = 0$, is investigated theoretically in this section. The process consists of direct and resonant channels as shown in Eq. (1), where the $1s^2 2p4p\,^1S_0^e$ autoionization level plays the role of an intermediate state mediating the resonance contribution.

The direct channels are initially neglected by setting all bound-free dipole elements to zero, $z_{J\kappa,1} = 0$, thus focusing only on the resonant component of photoionization, namely, the excitation-autoionization pathway. In the second stage of this section, direct photoionization channels are allowed to interfere with their resonant counterparts showcasing the final results for this study.

1. Resonant photoionization

In this work, resonant photoionization refers to the inverse of the dielectronic recombination process, consisting in photoexcitation of the $1s^2 2s2p\,^1P_1^o$ level to the quasibound $1s^2 2p4p\,^1S_0^e$ state via an external laser field, followed by autoionization as shown in the two-stage process presented in the initial scheme from Eq. (1). The direct photoionization of the $1s^2 2s2p\,^1P_1^o$ level together with its subsequent interference with the resonant channels is neglected in this section. The laser field also couples the quasibound level with

TABLE VIII. Requirements for a laser pulse acting on the $1s^2 2snp\,{}^1P_1^o$ level of the C^{2+} ion ($n \leqslant 5$), with the photon energy tuned to a bound-(quasi)bound resonant transition, to reach Rabi oscillation within the resonant Auger process (when direct channels are neglected) and threshold effects (when resonant contributions are ignored), respectively. The first column presents the autoionization states, the second and third columns give the required timescale, and the final eight columns show the required intensities in units of W/cm^2.

			Bound states							
			$2s2p\,{}^1P_1^o$		$2s3p\,{}^1P_1^o$		$2s4p\,{}^1P_1^o$		$2s5p\,{}^1P_1^o$	
Quasibound state	$\tau_{RA} = 1/\Gamma_r$	$\tau_{th} = 2\pi/\epsilon_r$	$I_{RA}^{\rm Rabi}$	I_{bf}^{th}	$I_{RA}^{\rm Rabi}$	I_{bf}^{th}	$I_{RA}^{\rm Rabi}$	I_{bf}^{th}	$I_{RA}^{\rm Rabi}$	I_{bf}^{th}
$2p4f\,{}^3F_2^e$	658.2 ps	17.23 fs	2.1×10^{8}	1.3×10^{14}	1.3×10^{7}	1.8×10^{13}	8.9×10^{7}	1.7×10^{14}	4.7×10^{5}	3.2×10^{12}
$2p4f\,{}^3D_2^e$	0.652 ps	9.618 fs		2.2×10^{14}	2.6×10^{11}	3.3×10^{13}	1.5×10^{12}	2.5×10^{14}	1.8×10^{8}	6.1×10^{12}
$2p4f\,{}^3D_1^e$	0.652 ps	9.551 fs		2.2×10^{14}	4.7×10^{13}	3.3×10^{13}		2.5×10^{14}	5.2×10^{8}	6.1×10^{12}
$2p4f\,{}^1D_2^e$	2.992 ps	9.149 fs	6.2×10^{11}	2.3×10^{14}	4.3×10^{8}	3.5×10^{13}	2.1×10^{9}	2.6×10^{14}	3.2×10^{8}	6.5×10^{12}
$2p4p\,{}^1S_0^e$	2.978 fs	8.527 fs	1.1×10^{16}	2.5×10^{14}	1.1×10^{18}	3.8×10^{13}	2.1×10^{15}	2.7×10^{14}		7.0×10^{12}

a set of odd-parity open channels via electric dipole interaction using $z_{\mathcal{FJK},r}$ matrix elements, giving rise to secondary photoelectrons of $\varepsilon_0 = 36.168$ eV energy, which compete with the autoionization process as shown in this scheme:

$$(C^{2+})^{**} + h\nu \rightarrow \begin{cases} C^{3+} + e^- + h\nu & \text{(autoionization)} \\ (C^3)^* + e^- & \text{(secondary photoionization).} \end{cases} \tag{42}$$

Since the photon energy is tuned to couple with a quasibound level slightly above the first ionization threshold, only ground-state C^{3+} ions can be generated in the subsequent autoionization process. Alternatively, photoionization of $1s^2 2p4p\,{}^1S_0^e$ generates C^{3+} ions in their ground state or two energetically available excited states, namely, $1s^2 2s\,{}^2S_{1/2}$ and $1s^2 2p\,{}^2P_{1/2}^o$, ${}^2P_{3/2}^o$. The corresponding (quasi)bound-free electric dipole moments are given in Table VI.

The excitation-autoionization field-induced dynamics is simulated by self-consistently solving Eqs. (28) and (29) for a 3-fs laser pulse for intensities in the 10^{12}–10^{17} W/cm^2 domain, while the $\delta_r = E_r - E^+ - \omega$ detuning is set to zero. The Auger electron and secondary photoelectron yields are then obtained using Eqs. (33) and (34), respectively. Local approximation results are also provided for comparison by using (35) and (36) for discrete levels in combination with (33) and (34) for continuum states. Auger electrons arising from the $1s^2 2p4p\,{}^1S_0^e \rightarrow [1s^2 2s + e^-(\epsilon s)]\,{}^1S_0^e$ process are only limited to s-type waves due to conservation laws of angular momentum and parity associated with an internal Coulomb interaction incapable of affecting the overall symmetries of the atomic system.

When neglecting the interference with direct photoionization channels together with the quasi(bound)-free transitions, the underlying system may effectively be treated as subjected to a resonant Auger process which requires the lifetime of Auger level $1/\Gamma_r \approx 3$ fs to be comparable to the timescale of driving field. According to Rohringer and Santra [6], the minimum intensity for the formation of bound-(quasi)bound Rabi oscillations within the resonant Auger process is

$$I_{RA}^{\rm Rabi} = \frac{1}{8\pi\alpha}\left(\frac{2\pi\Gamma_r}{|z_{r,1}|}\right)^2. \tag{43}$$

Table VIII gives the pulse temporal duration and intensity requirements for obtaining Rabi oscillations within the resonant Auger process provided direct photoionization channels are

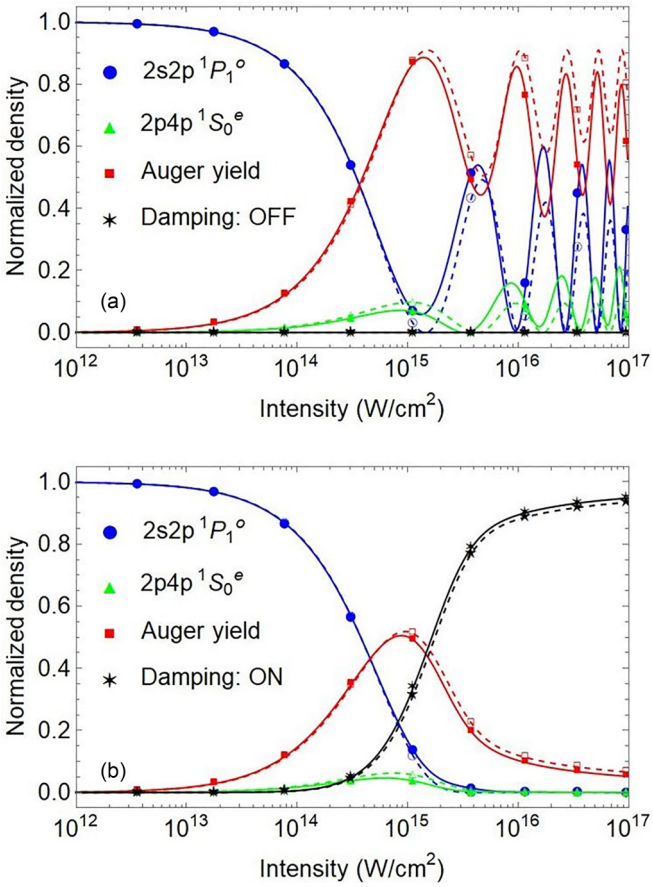

FIG. 6. Resonant photoionization of $1s^2 2s2p\,{}^1P_1^o$ via the doubly excited $1s^2 2p4p\,{}^1S_0^e$ level using a laser pulse of $h\nu = 35.683$ eV photon energy, 3 fs FWHM duration, and intensities in the 10^{12}–10^{17} W/cm^2 domain. The density of singly $1s^2 2s2p\,{}^1P_1^o$ (blue circles) and doubly $1s^2 2p4p\,{}^1S_0^e$ (green triangles) excited C^{2+} ions, the Auger yield (red squares), and secondary electron yield (black stars) (nonzero only when damping is turned on) are presented. Damping via (quasi)bound-free transitions is turned (a) off and (b) on. The corresponding open symbols linked by dashed lines represent results obtained by the local approximation calculation.

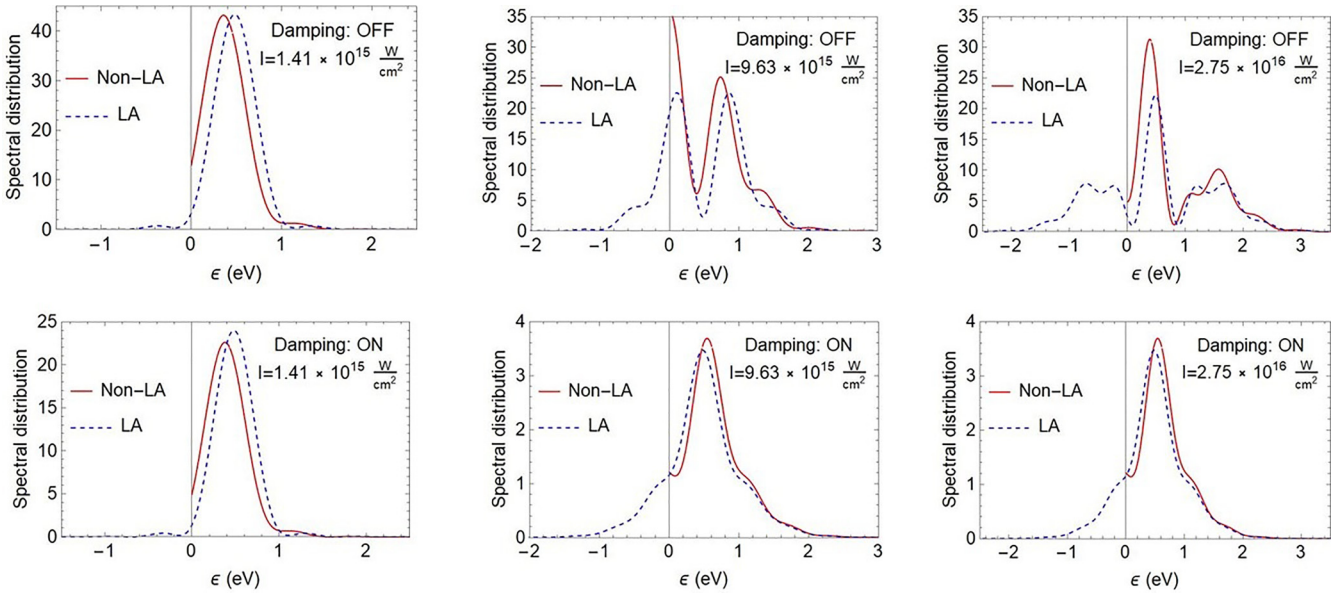

FIG. 7. Spectral distribution of Auger electrons as a result of resonant photoionization (photoexcitation autoionization) driven by a pulsed laser field of 3 fs FWHM duration for three intensity values 1.41×10^{15}, 9.63×10^{15}, and $2.75\times10^{16}\,\mathrm{W/cm^2}$. Dashed lines represent results obtained within the local approximation approach.

neglected. Alternatively, it also presents the necessary pulse timescale and intensities for exhibiting threshold effects in the absence of resonances. Ideally, only in the case of $1s^2 2p4p\,{}^1S_0^e$ do the requirements for both effects seem to overlap.

Figure 6 shows the evolution of population densities for the $1s^2 2s2p\,{}^1P_1^o$ excited state, the $1s^2 2p4p\,{}^1S_0^e$ autoionization level, and the Auger electron yield when using a 3 fs FWHM laser pulse of intensities 10^{12}–$10^{17}\,\mathrm{W/cm^2}$. Rabi cycles between bound and autoionizing discrete levels are formed and described in this section, not to be confused with bound-free Rabi oscillations induced by threshold effects.

Results given by the local approximation when damping is neglected [Fig. 6(a)] show that the resonant Auger process starts modulating the ionization dynamics at $I = 1.51\times10^{15}\,\mathrm{W/cm^2}$. The first and second local maxima in the Auger electron yield (dashed lines with open red squares) correspond to one and two complete Rabi cycles obtained at 1.06×10^{16} and $2.81\times10^{16}\,\mathrm{W/cm^2}$ laser intensity values, respectively. This is in accordance with the $1.1\times10^{16}\,\mathrm{W/cm^2}$ value presented in Table VIII. Threshold effects reduce the population of $1s^2 2p4p\,{}^1S_0^e$ (open green triangles) by 10% at around $3\times10^{14}\,\mathrm{W/cm^2}$, affecting the ionization process. These effects also change the position of local maxima within the Auger yield (solid line with closed red squares) to 9.63×10^{15} and $2.74\times10^{16}\,\mathrm{W/cm^2}$, respectively.

In Fig. 6(b) the coupling of the Auger level with odd open channels acts as a damping source for the Rabi cycles between bound and autoionization levels, completely nullifying them. Only at higher free-electron energies do the electric dipole elements between Auger and free states start decreasing enough to allow the formation of Rabi oscillations. Instead, this process gives rise to a high secondary photoelectron yield (black stars). Threshold effects produce no significant deviations from local approximation predictions on the electron yield in the case of resonant photoionization when damping is turned on.

The spectral distribution of Auger electrons is well represented by the local approximation approach as shown in Fig. 7, especially when damping is turned on. In the top row, threshold effects tend to redshift the Auger distributions while slightly enhancing them on the positive-energy axis. Overall, the modulations that occur when allowing nonlocal temporal contributions are not that different from those obtained within the local approximation and no new multipeak structures are created. Inclusion of damping (bottom row) only causes slight redshifting at $1.41\times10^{15}\,\mathrm{W/cm^2}$ and blueshifting at 9.63×10^{15} and $2.75\times10^{16}\,\mathrm{W/cm^2}$ for the Auger spectral distribution when compared to local approximation results.

Nonlocal effects within the time domain occur due to the intrinsic relations between field-driven photoionization and the distribution of ejected electrons. This intimate relation is disrupted within the perturbative description of resonant photoionization due to the spontaneous nature of the autoionization process. The cause for this disruption can be better understood by analyzing Eqs. (28) and (29), where the time-independent autoionization amplitude $V_{J\kappa,r}$ does not couple to the nonlocal temporal kernel within the argument of time integral. Since autoionization is the only process responsible for populating the free-electron states in resonant photoionization [see Eq. (33) with all $z_{J\kappa}$ dipole elements set to zero] there is no direct pathway that couples the nonlocal kernel to the spectral distribution of Auger electrons. One can infer that resonant contributions to photoionization are more robust to nonlocal temporal terms arising from cutoff conditions imposed on the free-electron energy domain.

The deviations in Auger electron yield between local and nonlocal approaches from Fig. 6 are mainly caused by the local approximation nonphysical distribution of free electrons below the first ionization threshold. Apart from the

lower-energy tail of the Auger electron spectral distribution, the local approach provides a decent approximate treatment for the resonant photoionization process irrespective of the resonance proximity to ionization thresholds. This no longer holds when including direct channels as shown in the following section.

2. Interference between direct and resonant channels

The photoionization of $1s^2 2s2p\,{}^1P_1^o$ belonging to the C^{2+} ion by using a pulsed laser field of 3 fs FWHM duration, tuned to the $2s2p$-$2p4p$ transition, accounting for both direct and resonant components is fully treated in this section. Nonresonant contributions lead to s- and d-wave ejected electrons arising from open channels of 0^e, 1^e, and 2^e partial symmetries, while Auger electrons only correspond to s waves due the fact that the autoionization process is mediated by internal Coulomb interactions leaving the system symmetries unchanged $1s^2 2p4p\,{}^1S_0^e \rightarrow [1s^2 2s + e^-(\epsilon s)]\,{}^1S_0^e$. For this reason, it is useful to divide the electron yield into pure photoelectrons given by open channels of 1^e and 2^e partial symmetries and joint direct plus resonant contributions that correspond to the s-wave electrons given by the only open channel of 0^e partial symmetry. This restricts the bound-(quasi)bound Rabi cycles to 0^e while allowing bound-free Rabi oscillations to occur at any partial symmetry. Equations (28) and (29) are numerically solved for $n = 32$ in order to simulate the photoionization dynamics and determine the densities for singly and doubly excited C^{2+} states. Electron yields are computed by solving Eqs. (33) and (34).

Results are shown in Fig. 8 with the damping turned off [Fig. 8(a)] and on [Fig. 8(b)]. In Fig. 8(a) the red squares (0^e) and orange diamonds ($1^2, 2^e$) have a similar shape and the effect of interference between direct and resonant contributions to 0^e partial symmetry only slightly shifts the position of local minima and maxima for the bound-free Rabi cycles. The shape of the electron yield corresponding to 0^e partial symmetry is clearly governed by the direct component and is only slightly affected by the excitation-autoionization contribution.

When turning on the damping process of the field-driven (quasi)bound-free interaction, the autoionization level is severely depopulated, leading to a significantly lower Auger electron yield. The damping completely nullifies the bound-(quasi)bound Rabi oscillations. This leads to a drop in the density of excited C^{2+} ions while also giving rise to a transfer of primarily ejected photoelectrons and Auger electrons into secondarily emitted photoelectrons (black). The local approximation yield for secondary electrons (black dashed line with stars) is significantly smaller than its nonlocal approach counterpart (black solid line with stars) due to the fact that the Auger level is no longer populated through Rabi oscillations.

The electrons emitted through the excitation-autoionization resonant pathway are also prone to laser-stimulated radiative recombination, thus repopulating the excited state of the C^{2+} ion, creating a new pathway that affects the field-induced bound-(quasi)bound dynamics. This is given by the interference terms I_{br} in Eqs. (28) and (29). Since damping nullifies bound-(quasi)bound Rabi oscillations, interference with direct photoionization also leads to the mitigation of threshold effects on the 0^e partial symmetry. This is shown by the closed red squares (0^e) in Fig. 8(b), where the number of threshold-induced bound-free Rabi oscillations has dropped significantly compared to closed orange diamonds (1^e, 2^e). It is worth mentioning that the local approximation severely undermines the production of secondary electrons (black stars) which in turn overestimates the primary electron yield (diamonds and squares), as can be seen in Fig. 8(b). Inclusion of above-threshold photoabsorption (free-free) processes would further enhance the transfer of primary photoelectrons or Auger electrons with energy around $\epsilon_r = 0.485$ eV to secondary electrons of $\varepsilon_0 = 36.168$ eV energy.

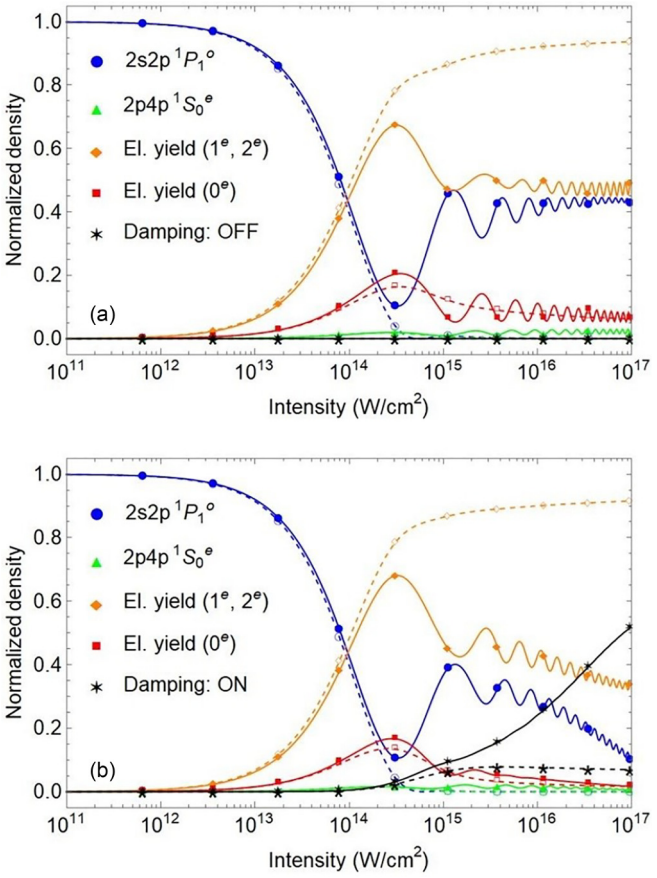

FIG. 8. Photoionization (direct plus resonant contributions) of the $1s^2 2s2p\,{}^1P_1^o$ level using a 3 fs FWHM laser pulse of $\omega = 35.683$ eV photon energy for intensity values in the 10^{11}–10^{17} W/cm^2 domain. The density of singly $1s^2 2s2p\,{}^1P_1^o$ (blue circles) and doubly $1s^2 2p4p\,{}^1S_0^e$ (green triangles) excited C^{2+} ions, the electron yield resulting from open channels of 0^e (red squares) and 1^e and 2^e (orange diamonds) partial symmetries, and secondary electron yield (black stars) (nonzero only when damping is turned on) are shown. Damping via (quasi)bound-free transitions is turned (a) off and (b) on. The corresponding open symbols linked by dashed lines represent results obtained by the local approximation calculation.

The spectral distribution of emitted electrons during the photoionization of the $1s^2 2s2p\,{}^1P_1^o$ state using a laser field of 3 fs FWHM duration, tuned at $\omega = 35.683$ eV, for three intensity values 1.41×10^{15}, 9.63×10^{15}, and 2.75×10^{16} W/cm^2, is given in Fig. 9. The secondary electron spectral distribution is

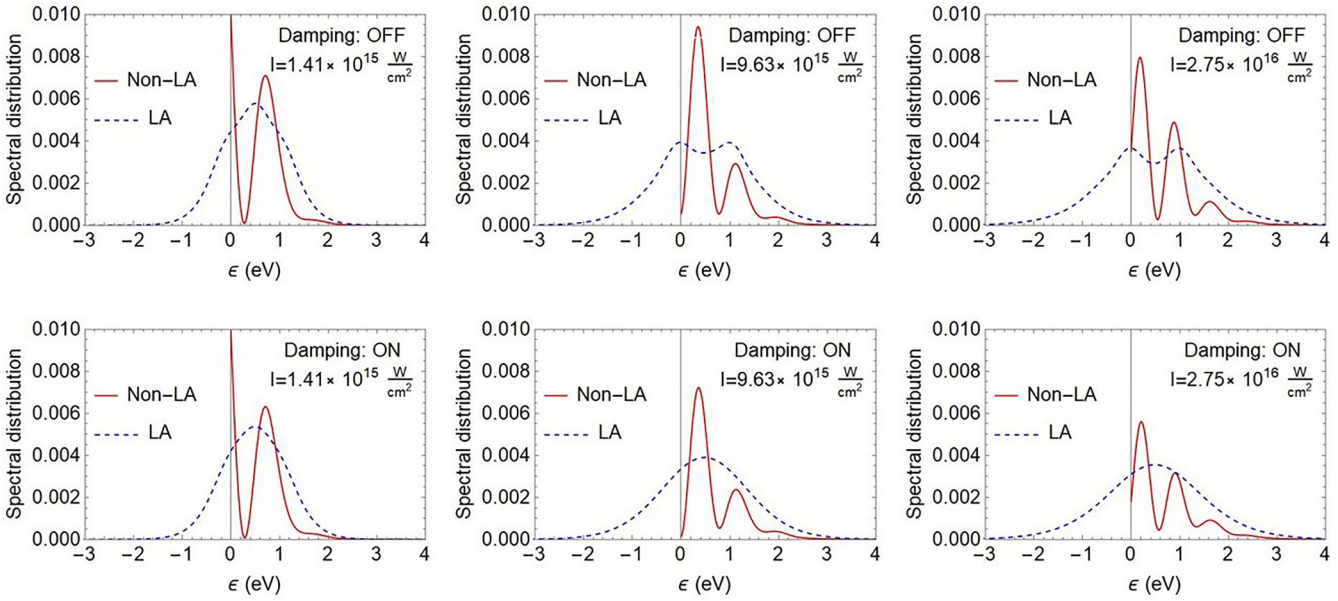

FIG. 9. Spectral distribution of ejected electrons, resulting from the even open channels of 0^e, 1^e, and 2^e partial symmetry, in the (direct plus resonant) photoionization of the $1s^2 2s2p\,{}^1P_1^o$ level using a laser field of 3 fs FWHM duration, tuned at $\omega = 35.683$ eV, for three intensity values 1.41×10^{15}, 9.63×10^{15}, and 2.75×10^{16} W/cm^2. Dashed lines represent results obtained by the local approximation approach.

symmetric around the $\varepsilon_0 = 36.168$ eV energy value, presenting no new insight into threshold effects.

Despite the fact that intensities have been chosen to maximize the resonant contributions, it is the threshold effects that clearly dominate the spectral distribution through direct channels. The present model predicts multipeak structures originating from the pulsed photoionization-stimulated radiative recombination cycles that occur during the field-ion interaction. Increasing the duration of laser pulses would result in more peaks within the spectral distribution; however, the difference between neighboring minima and maxima would drop. When the field temporal width far surpasses the photoelectron timescale, the differences between local maxima and minima are reduced up to the point where present spectra become indistinguishable from local approximation results. In contrast, if the pulse duration is instead shortened, the spectral distribution would continue to broaden, pushing peak structures into the forbidden threshold region while creating new ones above the central photoelectron energy, leading to larger deviations compared to a local approximation approach.

V. CONCLUSION

Time-dependent Dirac results predict the existence of bound-free Rabi oscillations within the laser-driven photoionization of the C III ion near the first ionization threshold. The origin of such an effect lies within the intrinsic relation between field-driven photoionization dynamics and photoelectron spectral distribution. As shorter, more intense laser pulses broaden the photoelectron distribution pushing its lower energetic tail into the forbidden region below threshold, nonlinear temporal terms within the evolution of atomic states are enhanced. Instead of a simple phenomenological decay predicted by the local approximation, the field-driven dynamics exhibits cycles of pulsed photoionization and stimulated radiative recombination. The field intensity necessary to cause the breakdown of the local approximation scales asymptotically with the photoelectron central energy at power 13/3, limiting the discrete-continuum Rabi oscillations to laser-driven photoionization near the first ionization threshold. The resonant coupling of the initial bound level to an autoionizing state hinders the intimate relation between laser-driven dynamics and ejected electron distribution due to the spontaneous nature of autoionization. The present results show that these nonlocal effects can heavily suppress the electron yield while significantly altering their spectral distribution.

ACKNOWLEDGMENT

This research was supported by Romanian Ministry of Research, Innovation and Digitalization under Romanian National Nucleu Program LAPLAS VII, Contract No. 30N/2023. Partial financial support from the Institute of Atomic Physics under Project No. F01/2020 is also acknowledged.

APPENDIX A: NONLOCAL KERNEL

This Appendix deals with the nonlocal kernel within the time integral argument obtained by analytically performing the integration over the free energy near the first ionization threshold:

$$K(t-t') = \frac{\sin[\epsilon_0(t-t')] + \sin[(n-1)\epsilon_0(t-t')]}{t-t'} - i\frac{\cos[\epsilon_0(t-t')] - \cos[(n-1)\epsilon_0(t-t')]}{t-t'}. \tag{A1}$$

It is assumed that the laser field starts acting on the atomic system at $t = 0$; thus, all $(-\infty, 0)$ contributions to the time integral are nullified. The two nonlocal terms comprising the kernel have finite limits at the origin:

$$\lim_{\tau\to 0} \frac{\sin(\alpha\tau)}{\tau} = \alpha, \tag{A2}$$

$$\lim_{\tau\to 0} \frac{\cos(\alpha\tau) - \cos(\beta\tau)}{\tau} = 0. \tag{A3}$$

Integration of these terms alone on the positive time domain also leads to well-known finite values

$$\int_0^\infty \frac{\sin(\alpha\tau)}{\tau} d\tau = \frac{\pi}{2}, \tag{A4}$$

$$\int_0^\infty \frac{\cos(\alpha\tau) - \cos(\beta\tau)}{\tau} d\tau = \ln\left(\frac{\beta}{\alpha}\right), \tag{A5}$$

where α and β are nonzero, positive, real numbers and ln stands for natural logarithm. This leads to

$$\int_0^\infty K(\tau) d\tau = \pi - i\ln(n-1). \tag{A6}$$

An issue arises if one extends the free-electron energy over the whole domain by taking the $n \to \infty$ limit, since the integral over cosine terms would diverge as $\lim_{n\to\infty} \ln(n-1)$. This appears due to the assumption that bound-free electric dipole elements are robust to energy variations around ϵ_0, which is not the case when extending the photoelectron energy domain to infinity. In linear response theory, sum rule techniques show that the dipole elements tend to decay with increasing excitation energy [66,67]. For this reason, one must consider the bound-free electric dipole elements' dependence on energy, which are proven to asymptotically behave as approximately $\epsilon^{-5/3}$ within the quasiclassical approximation [64,65]. The squared electric dipole elements belonging to the argument of the energy integral would behave as $\epsilon^{-10/3}$, which would in turn lead to the convergence of the time integral. Such an approach would require the knowledge of approximate analytic forms for the bound-free electric dipole matrix elements over the whole energy domain, in order to perform the photoelectron integration and eliminate the energy dependence from the terms used in the equation of motion for the bound state. However, the photoelectron distribution is fairly localized around the central energy ϵ_0, while the rest of the continuum states remain unpopulated. For this reason it is only useful to derive the equation of motion for finite values of n high enough to fully accommodate the photoelectron distribution obtained from the field-ion interaction. Numerical convergence is reached when increasing values for n no longer affect the photoionization dynamics.

In the special case of highly energetic photoelectrons, ϵ_0 can be formally extended to infinity such that the photoelectron distribution in no longer restricted in any way by the threshold region. In this particular case, choosing a symmetric energy domain ($n = 2$) becomes appropriate. The imaginary terms inside the braces go to zero while the sinc terms become highly oscillating effectively acting as parametrized Dirac δ functions when taking the energy limit to infinity. This allows nonlocal terms to be decoupled from the rest of time integral argument as shown by Demekhin and Cederbaum (see Appendix A in [8]), referring to this procedure as the local approximation. By employing this approach, Eq. (20) can be reduced to

$$\dot{c}_1(t) = -\pi \sum_{J\kappa} \left| z_{J\kappa,1} \frac{\mathcal{E}(t)}{2} \right|^2 c_1(t). \tag{A7}$$

APPENDIX B: DERIVING THE EQUATIONS FOR PHOTOIONIZATION NEAR A RESONANT STATE

The energy domain for Auger electrons is heavily restricted by the nearby ionization threshold and needs to be taken asymmetric with the upper margin parametrized to $n\epsilon_r$, where n is a real number which is to be determined later. In contrast, when the driving field couples the autoionization level situated at ϵ_r to odd-parity open channels distributed around the $\epsilon_r + \omega$ value, the (secondary) free electrons are situated away from any ionization threshold; thus the local approximation can be applied to model the secondary photoionization process with no restrictions. For example, the near-threshold condition for Auger electrons can be written as $E_r \gtrsim E^+$ or, by definition, $\epsilon_r \gtrsim 0$. Translated to the secondary electrons, this leads to $\varepsilon_0 = \epsilon_r + \omega \gtrsim \omega$. In the case of the $1s^2 2s 2p\, {}^1P_1^o$ state, one needs a laser frequency of $\omega = 35.7$ eV to photoexcite at roughly 0.5 eV above the first threshold where the quasibound states are situated. Ejected Auger electrons energy would be around the 0.5 eV value, while photoionization of such quasibound states would result in secondary photoelectrons centered at 36.2 eV, namely, two orders of magnitude higher and thus suitable for a local approximation treatment. The evolution equations for the expansion coefficients corresponding to discrete states are obtained by solving the time-dependent Dirac equation

$$\begin{aligned} i\dot{c}_1(t) = {} & d_r(t) e^{i\delta_r t} z_{1,r} \frac{\mathcal{E}^*(t)}{2} \\ & + \sum_{J,\kappa} z_{1,J\kappa} \frac{\mathcal{E}^*(t)}{2} \int_0^{n\epsilon_r} g_{J\kappa}(\epsilon, t) e^{-i(\epsilon-\epsilon_0)t} d\epsilon, \end{aligned} \tag{B1}$$

$$\begin{aligned} i\dot{d}_r(t) = {} & c_1(t) e^{-i\delta_r t} z_{r,1} \frac{\mathcal{E}(t)}{2} \\ & + \sum_{\mathcal{F},\mathcal{J},\mathcal{K}} \int_0^{2(\varepsilon_0 - \Delta^+_{\mathcal{F}})} h_{\mathcal{F}\mathcal{J}\mathcal{K}}(\varepsilon_{\mathcal{F}}, t) z_{r,\mathcal{F}\mathcal{J}\mathcal{K}} \frac{\mathcal{E}^*(t)}{2} \\ & \times e^{-i(\varepsilon_{\mathcal{F}} - \varepsilon_0 + \Delta^+_{\mathcal{F}})t} d\epsilon_{\mathcal{F}} \\ & + \sum_{J,\kappa} \int_0^{n\epsilon_r} g_{J\kappa}(\epsilon, t) V_{r,J\kappa} e^{-i(\epsilon - \epsilon_0 + \delta_r)t} \delta_{JJ_r} d\epsilon. \end{aligned} \tag{B2}$$

Open channels of even and odd parity are described by

$$\begin{aligned} i\dot{g}_{J\kappa}(\epsilon, t) = {} & c_1(t) z_{J\kappa,1} \frac{\mathcal{E}(t)}{2} e^{i(\epsilon-\epsilon_0)t} \\ & + d_r(t) V_{J\kappa,r} e^{i(\epsilon - \epsilon_0 + \delta_r)t} \delta_{JJ_r}, \end{aligned} \tag{B3}$$

$$i\dot{h}_{\mathcal{F}\mathcal{J}\mathcal{K}}(\varepsilon_{\mathcal{F}}, t) = d_r(t) z_{\mathcal{F}\mathcal{J}\mathcal{K},r} \frac{\mathcal{E}(t)}{2} e^{i(\varepsilon_{\mathcal{F}} - \varepsilon_0 + \Delta^+_{\mathcal{F}})t}. \tag{B4}$$

By performing formal time integration over Eqs. (B3) and (B4), one obtains

$$g_{J\kappa}(\epsilon,t) = -i\int_{-\infty}^{t} c_1(t')z_{J\kappa,1}\frac{\mathcal{E}(t')}{2}e^{i(\epsilon-\epsilon_0)t'} - iV_{J\kappa,r}\delta_{J_r\kappa}\int_{-\infty}^{t} d_r(t')e^{i(\epsilon-\epsilon_0+\delta_r)t'}dt', \quad \text{(B5)}$$

$$h_{\mathcal{F}\mathcal{J}\mathcal{K}}(\varepsilon_{\mathcal{F}},t) = -i\int_{-\infty}^{t} d_r(t')z_{\mathcal{F}\mathcal{J}\mathcal{K},r}\frac{\mathcal{E}(t')}{2}e^{i(\varepsilon_{\mathcal{F}}-\varepsilon_0+\Delta_{\mathcal{F}}^{+})t'}dt'. \quad \text{(B6)}$$

Substituting these free-state coefficients into the evolution equation for the discrete $1s^2 2snp\,{}^1P_1^o$ level gives

$$i\dot{c}_1(t) = d_r(t)e^{i\delta_r t}z_{1,r}\frac{\mathcal{E}^*(t)}{2} - \frac{i}{4}S_{bf}\mathcal{E}^*(t) \times \int_{-\infty}^{t} c_1(t')\mathcal{E}(t')\left(\int_0^{n\epsilon_r} e^{-i(\epsilon-\epsilon_0)(t-t')}d\epsilon\right)dt' - \frac{i}{2}I_{br}^*\mathcal{E}^*(t)\int_{-\infty}^{t} d_r(t') \times e^{-i\delta_r t'}\left(\int_0^{n\epsilon_r} e^{-i(\epsilon-\epsilon_0)(t-t')}d\epsilon\right)dt'. \quad \text{(B7)}$$

The time-dependent expansion coefficient corresponding to the autoionization level is governed by

$$i\dot{d}_r(t) = c_1(t)e^{-i\delta_r t}z_{r,1}\frac{\mathcal{E}(t)}{2} - i\frac{\Gamma_{sph}}{2}d_r(t) - i\frac{\Gamma_r}{2\pi}\int_{-\infty}^{t} d_r(t')\left(\int_0^{n\epsilon_r} e^{-i(\epsilon-\epsilon_0+\delta_r)(t-t')}d\epsilon\right)dt' - \frac{i}{2}I_{br}e^{-i\delta_r t}\int_{-\infty}^{t} c_1(t')\mathcal{E}(t') \times \left(\int_0^{n\epsilon_r} e^{-i(\epsilon-\epsilon_0)(t-t')}d\epsilon\right)dt', \quad \text{(B8)}$$

where the local approximation has been employed for describing the dynamics between the even-parity autoionization state and odd-parity open channels. Finally, replacing ϵ_0 with $\epsilon_r + \delta_r$ and performing the energy integration for both discrete states coefficients leads to Eqs. (28) and (29).

[1] P. V. Demekhin and L. S. Cederbaum, Dynamic Interference of Photoelectrons Produced by High-Frequency Laser Pulses, Phys. Rev. Lett. **108**, 253001 (2012).

[2] C. Weninger, M. Purvis, D. Ryan, R. A. London, J. D. Bozek, C. Bostedt, A. Graf, G. Brown, J. J. Rocca, and N. Rohringer, Stimulated Electronic X-Ray Raman Scattering, Phys. Rev. Lett. **111**, 233902 (2013).

[3] H. J. Wörner, H. Niikura, J. B. Bertrand, P. B. Corkum, and D. M. Villeneuve, Observation of Electronic Structure Minima in High-Harmonic Generation, Phys. Rev. Lett. **102**, 103901 (2009).

[4] E. W. B. Dias, H. S. Chakraborty, P. C. Deshmukh, S. T. Manson, O. Hemmers, P. Glans, D. L. Hansen, H. Wang, S. B. Whitfield, D. W. Lindle, R. Wehlitz, J. C. Levin, I. A. Sellin, and R. C. C. Perera, Breakdown of the Independent Particle Approximation in High-Energy Photoionization, Phys. Rev. Lett. **78**, 4553 (1997).

[5] E. P. Kanter, B. Krassig, Y. Li, A. M. March, P. Ho, N. Rohringer, R. Santra, S. H. Southworth, L. F. DiMauro, G. Doumy, C. A. Roedig, N. Berrah, L. Fang, M. Hoener, P. H. Bucksbaum, S. Ghimire, D. A. Reis, J. D. Bozek, C. Bostedt, M. Messerschmidt, and L. Young, Unveiling and Driving Hidden Resonances with High-Fluence, High-Intensity X-Ray Pulses, Phys. Rev. Lett. **107**, 233001 (2011).

[6] N. Rohringer and R. Santra, Resonant Auger effect at high x-ray intensity, Phys. Rev. A **77**, 053404 (2008).

[7] N. Rohringer and R. Santra, Strongly driven resonant Auger effect treated by an open-quantum-system approach, Phys. Rev. A **86**, 043434 (2012).

[8] P. V. Demekhin and L. S. Cederbaum, Strong interference effects in the resonant Auger decay of atoms induced by intense x-ray fields, Phys. Rev. A **83**, 023422 (2011).

[9] P. V. Demekhin and L. S. Cederbaum, Quantum oscillations between close-lying states mediated by the electronic continuum in intense high-frequency pulses, Phys. Rev. A **91**, 013417 (2015).

[10] L. S. Cederbaum and W. Domcke, Local against non-local complex potential in resonant electron-molecule scattering, J. Phys. B **14**, 4665 (1981).

[11] W. Domcke, Theory of resonance and threshold effects in electron-molecule collisions: The projection-operator approach, Phys. Rep. **208**, 97 (1991).

[12] H. S. Chakraborty, D. L. Hansen, O. Hemmers, P. C. Deshmukh, P. Focke, I. A. Sellin, C. Heske, D. W. Lindle, and S. T. Manson, Interchannel coupling in the photoionization of the *M* shell of Kr well above threshold: Experiment and theory, Phys. Rev. A **63**, 042708 (2001).

[13] D. L. Hansen, O. Hemmers, H. Wang, D. W. Lindle, P. Focke, I. A. Sellin, C. Heske, H. S. Chakraborty, P. C. Deshmukh, and S. T. Manson, Validity of the independent-particle approximation in x-ray photoemission: The exception, not the rule, Phys. Rev. A **60**, R2641(R) (1999).

[14] H. S. Chakraborty, P. C. Deshmukh, and S. T. Manson, Interchannel-coupling effects in the spin polarization of energetic photoelectrons, Phys. Rev. A **67**, 052701 (2003).

[15] M. Baghery, U. Saalmann, and J. M. Rost, Essential Conditions for Dynamic Interference, Phys. Rev. Lett. **118**, 143202 (2017).

[16] S. Schippers, M. Schnell, C. Brandau, S. Kieslich, A. Muller, and A. Wolf, Experimental Mg IX photorecombination rate coefficient, Astron. Astrophys. **421**, 1185 (2004).

[17] S. Schippers, D. Bernhardt, A. Müller, C. Krantz, M. Grieser, R. Repnow, A. Wolf, M. Lestinsky, M. Hahn, O. Novotny, and D. W. Savin, Dielectronic recombination of xenonlike tungsten ions, Phys. Rev. A **83**, 012711 (2011).

[18] N. R. Badnell, C. P. Ballance, D. C. Griffin, and M. O'Mullane, Dielectronic recombination of $W^{20+}(4d^{10}4f^8)$: Addressing the half-open f shell, Phys. Rev. A **85**, 052716 (2012).

[19] A. Bar-Shalom, M. Klapisch, and J. Oreg, Electron collision excitations in complex spectra of ionized heavy atoms, Phys. Rev. A **38**, 1773 (1988).

[20] J. Oreg, W. H. Goldstein, M. Klapisch, and A. Bar-Shalom, Autoionization and radiationless electron capture in complex spectra, Phys. Rev. A **44**, 1750 (1991).

[21] C. H. Zhang and U. Thumm, Electron-ion interaction effects in attosecond time-resolved photoelectron spectra, Phys. Rev. A **82**, 043405 (2010).

[22] J. Vos, L. Cattaneo, S. Patchkovskii, T. Zimmermann, C. Cirelli, M. Lucchini, A. Kheifets, S. Landsman, and U. Keller, Orientation-dependent stereo Wigner time delay and electron localization in a small molecule, Science **360**, 1326 (2018).

[23] J. Liang, Y. Zhou, J. Tan, M. He, Q. Ke, Y. Zhao, M. Li, W. Jiang, and P. Lu, Low-energy photoelectron interference structure in attosecond streaking, Opt. Express **27**, 37736 (2019).

[24] U. Schramm, J. Berger, M. Grieser, D. Habs, E. Jaeschke, G. Kilgus, D. Schwalm, A. Wolf, R. Neumann, and R. Schuch, Observation of Laser-Induced Recombination in Merged Electron and Proton Beams, Phys. Rev. Lett. **67**, 22 (1991).

[25] F. B. Yousif, P. Van der Donk, Z. Kucherovsky, J. Reis, E. Brannen, J. B. A. Mitchell, and T. J. Morgan, Experimental Observation of Laser-Stimulated Radiative Recombination, Phys. Rev. Lett. **67**, 26 (1991).

[26] C. Wesdorp, F. Robicheaux, and L. D. Noordam, Field-Induced Electron-Ion Recombination: A Novel Route towards Neutral (Anti-)matter, Phys. Rev. Lett. **84**, 3799 (2000).

[27] M. L. Rogelstad, F. B. Yousif, T. J. Morgan, and J. B. Mitchell, Stimulated radiative recombination of H^+ and He^+, J. Phys. B **30**, 3913 (1997).

[28] S. Mannervik, D. DeWitt, L. Engstrom, J. Lidberg, E. Lindroth, R. Schuch, and W. Zong, Strong Relativistic Effects and Natural Linewidths Observed in Dielectronic Recombination of Lithiumlike Carbon, Phys. Rev. Lett. **81**, 313 (1998).

[29] K. Abrahamsson, G. Andler, L. Bagge, E. Beebe, P. Carle, H. Danared, S. Egnell, K. Ehrnsten, M. Engstrom, C. J. Herrlander, J. Hilke, J. Jeansson, A. Kallberg, S. Leontein, L. Liljeby, A. Nilsson, A. Paal, K. G. Rensfelt, U. Rosengard, A. Simonsson *et al.*, CRYRING—A synchrotron, cooler and storage ring, Nucl. Instrum. Methods Phys. Res. Sect. B **79**, 269 (1993).

[30] A. Derevianko, V. A. Dzuba, and M. G. Kozlov, Relativistic many-body calculation of low-energy dielectronic resonances in Be-like carbon, Phys. Rev. A **82**, 022720 (2010).

[31] R. Mann, High-resolution K and L Auger electron spectra induced by single- and double-electron capture from H_2, He, and Xe atoms to C^{4+} and C^{5+} ions at 10–100-keV energies, Phys. Rev. A **35**, 4988 (1987).

[32] Z. Chen and C. D. Lin, Calculations of energies of intrashell doubly excited states of beryllium-like ions, J. Phys. B **22**, 2875 (1989).

[33] H. Bachau, P. Galan, F. Martin, A. Riera, and M. Yanez, Resonance parameters and properties of beryllium-like doubly excited states: $4 \leqslant Z \leqslant 10$, At. Data Nucl. Data Tables **44**, 305 (1990).

[34] M. Cornille, J. Dubau, and U. I. Safronova, Energies and autoionization rates for Be-like systems. Comparison of two methods: AUTOLSJ and MZ, Phys. Scr. **48**, 546 (1993).

[35] P. Quinet, Predicted term energies, wavelengths and oscillator strengths for transitions involving high-nl Rydberg states in C II, C III and C IV, Astron. Astrophys. Suppl. Ser. **129**, 603 (1998).

[36] W. J. Pong and Y. K. Ho, Doubly-excited states of beryllium-like ions, Phys. Scr. **61**, 690 (2000).

[37] Y. Shiina, R. Kinoshita, S. Funada, M. Matsuda, M. Imai, K. Kawatsura, M. Sataka, K. Sasa, and S. Tomita, Measurement of Auger electrons emitted through Coster-Kronig transitions under irradiation of fast C_2^+ ions, Nucl. Instrum. Methods Phys. Res. Sect. B **460**, 30 (2019).

[38] V. Stancalie, Contribution to the theoretical investigation of electron and photon interaction with carbon atom and its ions, J. Phys.: Conf. Ser. **576**, 012010 (2015).

[39] V. Stancalie, Singly resonant multiphoton processes involving autoionizing states in the Be-like C III ion, Symmetry **14**, 2528 (2022).

[40] V. Stancalie, Static and dynamic polarizability for C^{2+} in Rydberg states, AIP Adv. **5**, 077186 (2015).

[41] A. Müller, R. A. Phaneuf, A. Aguilar, M. F. Gharaibeh, A. S. Schlachter, I. Alvarez, C. Cisneros, G. Hinojosa, and B. M. McLaughlin, Photoionization of C^{2+} ions, Nucl. Instrum. Methods Phys. Res. Sect. B **205**, 301 (2003).

[42] A. Muller, A. Schippers, A. Aguilar, M. E. Bannister, J. Bozek, C. Cisneros, A. M. Covington, G. H. Dunn, M. F. Charaibeh, G. Hinojosa, S. Ricz, A. S. Schlachter, and R. A. Phaneuf, Time-reversal studies in photorecombination and photoionization experiments with ion beams, AIP Conf. Proc. **680**, 191 (2003).

[43] A. Müller, R. A. Phaneuf, A. Aguilar, M. F. Gharaibeh, A. S. Schlachter, I. Alvarez, C. Cisneros, G. Hinoja, and B. M. McLaughlin, Photoionization of C^{2+} ions: Time-reversed recombination of C^{3+} with electrons, J. Phys. B **35**, L137 (2002).

[44] D.-S. Kim and T. M. Steven, Photoionization of the ground state of the Be-like C^{2+} ion leading to $C^{3+}2l$ and $3l$ states, J. Phys. B **37**, 4707 (2004).

[45] D.-S. Kim and Y. S. Kim, Characteristics of photoionization in the XUV domain for the excited $1s^22s2p\,^{1,3}P^o$ states of the Be-like C^{2+} ion, J. Phys. B **40**, 3807 (2007).

[46] V. Stancalie, Photoionization dynamics of the C^{2+} ion in Rydberg states, Eur. Phys. J. D **68**, 349 (2014).

[47] G. Hofmann, A. Muller, K. Tinschert, and E. Salzborn, Indirect processes in the electron-impact ionization of Li-like ions, Z. Phys. D **16**, 113 (1990).

[48] H. Knopp, H. Teng, S. Ricz, S. Schippers, and A. Muller, Interference in electron-impact ionization of C^{3+} ions: Unified R-matrix calculation and experiment, Phys. Scr. **T92**, 379 (2001).

[49] V. Stancalie, State selective photo-recombination cross sections in Be-like C and Al ions, Eur. Phys. J. D **67**, 223 (2013).

[50] S. Schippers, A. Muller, G. Gwinner, J. Linkemann, A. A. Saghiri, and A. Wolf, Storage ring measurement of the C IV recombination rate coefficient, Astrophys. J. **555**, 1027 (2001).

[51] M. S. Pindzola, S. D. Loch, and F. Robicheaux, Dielectronic recombination in C^{3+} above and below the ionization threshold, Phys. Rev. A **83**, 042705 (2011).

[52] M. H. Chen, Dielectronic satellite spectra of Li-like ions, At. Data Nucl. Data Tables **37**, 419 (1987).

[53] U. Safronova, T. Kato, and M. Ohira, Dielectronic recombination rate coefficients to the excited states of C III from C IV, J. Quant. Spectrosc. Radiat. Transfer **58**, 193 (1997).

[54] K. Berrington, J. Pelan, and L. Quigley, *R*-matrix calculations of C III bound and continuum fine-structure states, Phys. Scr. **57**, 549 (1998).

[55] A. K. Pradhan, G. X. Chen, S. N. Nahar, and H. L. Zhang, Relativistic Fine Structure and Resonance Effects in the Electron-Ion Recombination and Excitation of (e+ C IV), Phys. Rev. Lett. **87**, 183201 (2001).

[56] J. Rothhardt, M. Bilal, R. Beerwerth, A. V. Volotka, V. Hilbert, T. Stohlker, S. Fritzsche, and J. Limpert, Lifetime measurements of ultrashort–lived excited states in Be-like ions, X-Ray Spectrom. **49**, 165 (2020).

[57] A. Kramida, Y. Ralchenko, J. Reader, and NIST ASD Team, NIST Atomic Spectra Database, version 5.10, available at http://physics.nist.gov/asd (National Institute of Standards and Technology, Gaithersburg, 2022).

[58] M. F. Gu, Flexible atomic code, Can. J. Phys. **86**, 675 (2008).

[59] C. Iorga and V. Stancalie, Linear polarization of the dielectronic recombination $K\alpha$ satellite lines in Li-like Au^{76+}, J. Quant. Spectrosc. Radiat. Transfer **224**, 206 (2019).

[60] C. Iorga and V. Stancalie, Energy levels, oscillator strengths, radiative transition probabilities, level lifetimes and electron-impact excitation rate coefficients for Ne-like Mo XXXIII, At. Data Nucl. Data Tables **131**, 101286 (2020).

[61] U. Fano, Effects of configuration interaction on intensities and phase shifts, Phys. Rev. **124**, 1866 (1961).

[62] C. Iorga and V. Stancalie, The study of core-valence and core-core correlation effects on the radiative properties along the magnesium isoelectronic sequence, At. Data Nucl. Data Tables **123–124**, 313 (2018).

[63] I. P. Grant, in *Relativistic Quantum Theory of Atoms and Molecules* (Springer, New York, 2007), pp. 1–797.

[64] N. B. Delone, S. P. Goreslavsky, and V. P. Krainov, Dipole matrix elements in the quasi-classical approximation, J. Phys. B **27**, 4403 (1994).

[65] K. Yamanouchi, S. L. Chin, P. Agostini, and G. Ferrante, in *Progress in Ultrafast Intense Laser Science I*, Springer Series in Chemical Physics (Springer, Berlin, 2006), Vol. 84, pp. 1–329.

[66] V. Baran, D. I. Palade, M. Colonna, M. Di Toro, A. Croitoru, and A. I. Nicolin, Collectivity of the pygmy dipole resonance within schematic Tamm-Dancoff approximation and random-phase approximation models, Phys. Rev. C **91**, 054303 (2015).

[67] D. I. Palade and V. Baran, N-block separable random phase approximation: Dipole oscillations in sodium clusters and C_{60} fullerene, J. Phys. B **49**, 175101 (2016).